Universität Bremen

ALFRED-WEGENER-INSTITUT
HELMHOLTZ-ZENTRUM FÜR POLAR-
UND MEERESFORSCHUNG

Viscous Plastic Sea Ice Models at Very High Resolution

Master's Thesis in the Postgraduate Programme
Environmental Physics (PEP)

Nils Hutter

First examiner: Prof. Dr. Thomas Jung
Second examiner: Prof. Dr. Peter Lemke
Supervisor: Dr. Martin Losch

date of submission	30.9.2015
author's name	Nils Hutter
date of birth	8.10.1988
matriculation number	

Abstract

The Arctic sea ice cover is crisscrossed by leads and pressure ridges, often referred to as linear kinematic features (LKFs). Leads are areas of open ocean in the sea ice cover. As such they play a crucial role in the Arctic climate system because they accommodate large amounts of the Arctic heat loss and thus enable sea ice formation. Hence a proper representation of LKFs in a climate model is expected to improve its overall performance.

So called viscous-plastic (VP) sea ice models are used in most climate models and are thought to represent the sea ice accurately on large scales. Here, the spatial resolution is pushed to scales of 1 km to show leads emerging in a VP sea ice model at those very high resolutions. In order to avoid unnecessary computational limits, first steps are taken with an idealized environment set up implemented with the MIT General Circulation Model (MITgcm). The modeled sea ice deformation is compared to observational data by a statistical analysis and using the fractal characteristics of sea ice deformation. The probability distributions of the deformation rates have power-law tails in attraction of the Lévy law at high resolutions. This implies that, the localization of strain rate events increases with refining spatial resolution. In addition, it is found that the ice strength depends on the spatial resolution. So that, the ice strength P^* needs to be reduced with increasing grid size to obtain comparable dynamic behavior of the modeled ice. Moreover, spatial and temporal scaling laws are explored for sea ice deformation. By increasing the resolution of the wind forcing more small scale strain rate events are induced in the ice leading to a better agreement with fractal characteristics of spatial scaling laws. So that VP becomes comparable to the elasto brittle (EB) rheology. Areas of low sea ice concentration dominate temporal scaling laws. In dense pack ice, deformation events persist over a period of ten days at small spatial scales.

In the second part the predictability of the modeled leads is investigated. The position of modeled LKFs is strongly sensitive to uncertainties in the wind forcing and initial conditions. Uncertainties in satellite sea ice products and weather forecast lead to a predictive skill of 1 to 2 days.

Contents

Chapter 1

Introduction

The Arctic sea ice is not a homogeneous ice cover but an aggregation of ice floes of various sizes. Driven by winds and ocean currents, the ice floes fracture (Marko and Thomson, 1977) and move in a general circulation as well as relative to each other (Thorndike and Colony, 1982). The collision of two ice floes forms pressure ridges, whereas diverging ice floes leave strips of open ocean, called leads. These features occur on scales from a few meters up to basin scale (Schulson and Duval, 2009), and due to their dynamic nature they are often referred to as *Linear Kinematic Features* (LKF) (Kwok, 2001).

Although leads are covering only a small area fraction of 0.4 % in winter (Kwok, 2002), they accommodate many processes relevant for the Arctic climate: In wintertime sea ice acts as an insulator between the cold atmosphere and the warm ocean. Half of the oceanic heat loss to the atmosphere takes place directly in leads (Heil and Hibler, 2002). The cooling of the surface water induces new sea ice growth, which influences the salinity of the ocean underneath by brine rejection and modifies the heat budget (Maykut, 1982). In summertime the increased absorption of shortwave radiation caused by the decrease of albedo in leads is dominant, which results in a warming of the ocean (Maykut, 1986). The temperature rise melts the sea ice exposing further dark ocean and shortens the freezing period. This forms the positive sea ice-albedo feedback (Curry et al., 1995). The increased solar radiation penetrating the water surface intensifies the biological activity in the Arctic ocean (Hill

and Cota, 2005), so that leads are of crucial importance for the Arctic ecosystem (Stirling, 1997). Given these complex processes in leads, a proper representation of LKFs in a climate model is expected to improve its overall performance.

So called *viscous-plastic* (VP) sea ice models (Hibler, 1979) are used in most climate system models and are thought to well represent the sea ice in large scale velocity fields (Lindsay et al., 2003; Kwok et al., 2008) and spatial pattern of sea ice thickness (Kreyscher et al., 2000). Studying the deformation rates in VP models, Lindsay et al. (2003) and Kwok et al. (2008) described large differences between model and satellite measurements, which originate from too homogeneous velocity fields in the model. The lack of small scale spatial variations results in low deformation rates, which depend in the spatial derivative of the velocity fields. Girard et al. (2009) analyzed the deformation properties of VP models more explicitly at a grid size of 12 km, and explored the scaling characteristics and multi-fractality of deformation rates. Thereby significant discrepancies were revealed compared to scaling laws of sea ice deformation deduced from satellite data (Marsan et al., 2004; Stern and Lindsay, 2009) and buoy trajectories (Rampal et al., 2008), in particular because the extreme localization of large strain rate events, like structural failure on sub-grid scale, is not properly represented by the model (Girard et al., 2009). With increased the resolution, the viscous-plastic rheology is in principle able to reproduce LKFs (Overland and Ukita, 2000; Maslowski and Lipscomb, 2003). This gives rise to the following questions:

- Does a better representation of local failure zones by increasing spacial resolution lead to more realistic statistics of sea ice deformation? Does a high resolution VP model reproduce observational scaling laws for sea ice deformation, similar to the elasto-brittle rheology (Girard et al., 2011; Bouillon and Rampal, 2015b)?

- Furthermore does the density of leads and cracks in the model gradually vary with increasing resolution, or does a sharp transition to a LKF resolving regime exists? If so how are the scaling properties of modeled sea ice deformation influenced by different types of transitions?

2

- Do the modeled LKFs coincide in multi fractal characteristics with observations of sea ice deformation (Marsan et al., 2004; Bouillon and Rampal, 2015a)?

- Finally does the existence of LKFs cause enhanced heat transport and growth rates and thus might change the performance of the sea ice component in climate models?

In my work I address some of these questions with a resolution study on viscous-plastic sea ice models performed with the help of the Massachusetts Institute of Technology general circulation model (MITgcm). Starting with a coarse resolution of 10 km as commonly used in climate models, the resolution is gradually refined to scales of 1 km. To reduce computation time, an idealized environment of quadratical shape with closed boundary conditions is used imitating an ocean basin surrounded by coasts. The ice motion and deformation is initiated with idealized atmospheric wind forcing, that is given by the passage of idealized low and high pressure systems, as well as with reanalysis wind fields. In the future one can generalize this work to realistic geometries. Based on the modeled sea ice motion, strain rates are calculated and the resulting sea ice deformation is analyzed with respect to scaling laws. The progress in resolving LKFs with higher resolution is evaluated by a comparison of the deduced scaling laws with observational scaling laws (Marsan et al., 2004; Rampal et al., 2008; Stern and Lindsay, 2009; Hutchings et al., 2011), and an inspection of the multi fractal characteristics.

In times of reducing sea ice the Trans-Arctic shipping will intensify (Smith and Stephenson, 2013). As ships can travel in leads more easily, a forecast of LKFs is of particular interest for scientific cruises and economic stakeholders. This gives rise to the question, whether the predictability is sufficiently high to forecast positions of leads and how sensitive the modeled LKFs are to uncertainties in forcing and initial conditions? The second part of the thesis addresses these questions with a sensitivity study of the modeled LKFs. To this end, the wind forcing and initial conditions are perturbed to examine the predictability of modeled leads.

Chapter 2

Sea Ice Dynamics

2.1 Momentum Balance of Sea Ice

Sea ice covers the Arctic ocean with an extent of some thousand kilometers, whereas its thickness, the vertical extent, scales to few meters. In particular the vertical velocities in sea ice are small and the vertical gradients of the horizontal ice velocities are negligible. Thus the integration over the vertical axis leads to a 2D-description of ice moving on the rotating Earth. The momentum balance of sea ice (normalized by area) is

$$m\left(\frac{\partial \mathbf{u}}{\partial t} + \mathbf{u} \cdot \nabla \mathbf{u}\right) = -mf\mathbf{k} \times \mathbf{u} + \tau_a + \tau_o - mg\nabla H + \nabla \cdot \sigma, \qquad (2.1)$$

where the left hand side describes the change in momentum of the ice with $m = \rho\, h$ as the mass per unit area of the ice (ρ is the ice density and h the ice thickness) and the horizontal velocity vector $\mathbf{u}$. Due to scale analysis the advection term $\mathbf{u} \cdot \nabla \mathbf{u}$ is neglected. On the right hand side all forces acting on the ice are summarized: the Coriolis force given by the Coriolis parameter f and the cross product of the unit vector normal to the surface $\mathbf{k}$ with $\mathbf{u}$, the atmospheric τ_a and oceanic stress τ_o acting on the ice due to winds and currents, the gravitational force due to the surface tilt described by the gravitational constant g and the surface height H, and the force caused by the divergence of the internal stress tensor σ (Hibler, 1979; Feltham, 2008).

The atmospheric and oceanic stresses are approximated by quadratic drag laws

$$\tau_a\left(\mathbf{u}\right) = \rho_a C_a \left|\mathbf{U_a} - \mathbf{u}\right| \mathbf{R}_a \left(\mathbf{U_a} - \mathbf{u}\right), \tag{2.2}$$

$$\tau_o\left(\mathbf{u}\right) = \rho_o C_o \left|\mathbf{U_o} - \mathbf{u}\right| \mathbf{R}_o \left(\mathbf{U_o} - \mathbf{u}\right), \tag{2.3}$$

$$\mathbf{R}_i = \begin{bmatrix} \cos\theta_i & -\sin\theta_i \\ \sin\theta_i & \cos\theta_i \end{bmatrix}, \quad i = a, o \tag{2.4}$$

where $\mathbf{u}$ is the ice velocity, ρ_i is the density, θ_i the boundary layer turning angle, $\mathbf{R}_i$ the related rotation matrix, and $\mathbf{U}_i$ the velocity of the atmosphere $(i = a)$ respective the ocean $(i = o)$ (Leppäranta, 2011). The latter are used to estimate the influence of the unresolved Ekman layer; in case of a resolved Ekman layer θ is zero.

With the parametrization (2.2) and (2.3) $\mathbf{u}$ and σ in (2.1) are the only unknown quantities giving six unknowns (respective five unknowns in case of an isotropic material and thus symmetric stress tensor) with two equations. Therefore additional constraints are needed to solve the set of equations: the sea ice rheology.

2.2 Sea Ice Rheology

The relationship between the stress tensor σ and the horizontal velocity $\mathbf{u}$ is given by the sea ice rheology, which relates the stress tensor σ to the sea ice strain rate $\dot{\epsilon}$ given by the spacial derivatives of the velocity $\mathbf{u}$ as,

$$\dot{\epsilon}_{ij} = \frac{1}{2}\left(\frac{\partial \mathbf{u}_i}{\partial x_j} + \frac{\partial \mathbf{u}_j}{\partial x_i}\right), \quad i, j \in [1, 2]. \tag{2.5}$$

Different rheologies for sea ice have been suggested using in situ measurements of internal ice stress from several field experiments. All of them share common properties of sea ice deformation. The deformation is caused by the different stress states measured in the ice: tensile load, compression and shear. Thereby the resistance of ice is weakest against tension and strongest against compression. The resistance of ice against tension is notably low and mostly neglected in sea ice rheologies permitting free drift for divergent states.

The most used rheology in climate models is the viscous-plastic rheology introduced by Hibler (1979). This rheology is also used in this study.
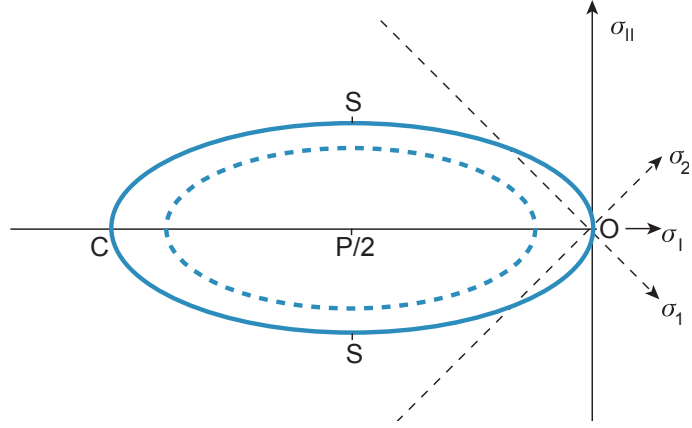
Figure 2.1: Elliptic yield curve: Stress states lying on the solid line lead to plastic flow. C represents pure convergence, O pure divergence and S pure shear (Feltham, 2008).

2.2.1 Viscous-Plastic Rheology

The viscous-plastic rheology distinguishes between two different regimes: the plastic regime for high stress states and viscous regime for subcritical stress states approximating that multiple plastic failures on sub-grid scale act together as viscous (Hibler, 1977). Assuming ice to be an isotropic material, the stress tensor σ_{ij} and the strain rate $\dot{\epsilon}_{ij}$ are linked by a non-linear viscous-plastic constitutive law given by the Reiner-Rivlin form (Hibler, 1979),

$$\sigma_{ij} = 2\,\eta\,(\dot{\epsilon}_{ij}, P)\,\dot{\epsilon}_{ij} + [\zeta\,(\dot{\epsilon}_{ij}, P) - \eta\,(\dot{\epsilon}_{ij}, P)]\,\dot{\epsilon}_{kk}\,\delta_{ij} - \frac{P}{2}\,\delta_{ij}, \tag{2.6}$$

where ζ and η are the nonlinear bulk and shear viscosities, P is the maximum compressive strength of ice and δ_{ij} is the Kronecker delta.

For practical reasons Hibler (1979) chose ζ and η so that all plastic stress states lie on an elliptic yield curve,

$$\zeta = \frac{P}{2}\Delta, \tag{2.7}$$

$$\eta = \frac{\zeta}{e^2}, \tag{2.8}$$

$$\Delta = \left[\left(\dot{\epsilon}_{11}^2 + \dot{\epsilon}_{22}^2\right)\left(1 + e^{-2}\right) + 4\,e^{-2}\dot{\epsilon}_{12}^2 + 2\,\dot{\epsilon}_{11}\dot{\epsilon}_{22}\left(1 - e^{-2}\right)\right]^{\frac{1}{2}}, \tag{2.9}$$

where e is the ratio between the major and the minor axis of the ellipse. The material behavior of sea ice, which is the strongest in compression, strong in shear

and weak in tension, is well represented in such a yield curve (Fig. 2.1). To show this the two stress invariants σ_I for normal stress and σ_{II} for maximum shear have to be considered,

$$\sigma_I = \frac{1}{2} \left(\sigma_1 + \sigma_2 \right), \tag{2.10}$$

$$\sigma_{II} = \frac{1}{2} \left(-\sigma_1 + \sigma_2 \right), \tag{2.11}$$

with the principal stresses σ_1 and σ_2. Stress states lying on the elliptic yield curve are characterized by irreversible plastic deformations whereas stress states lying inside the yield curve are related to viscous flow or creep.

Finally, Hibler (1979) defined a thickness distribution of sea ice consisting of only two thickness classes: ice of the mean thickness h covering an area fraction of A and thin ice as well as open ocean covering $(1 - A)$ of the area. To couple the ice dynamics with the thickness of ice, a parameterization of the ice strength is introduced depending on h and A

$$P = P^* h \, \exp \left[-C \left(1 - A \right) \right], \tag{2.12}$$

where P^* and C are fixed empirical constants. Thus obviously, the ice gets weaker by increasing the amount of thin ice $(1 - A)$ and strengthens by a rising amount of thick ice A and ice thickness h respectively.

2.2.2 Other Rheologies

As part of the Arctic Ice Dynamics Joint Experiment (AIDJEX) Coon et al. (1974) proposed a rheology assuming elastic-plastic behavior of sea ice because subcritical stress propagates over far distances in the ice. However, the subcritical elastic deformation requires the computation of a stress-free reference run with only plastic deformation to calculate the strain rate for each time step and thus is computationally very expensive.

Since then various rheologies and modifications have been presented, from which two related to the modeling of LKFs are outlined: Hutchings et al. (2005) modeled LKFs using the modified Coulomb rheology and Girard et al. (2011) showed that

the elasto-brittle rheology reproduces scaling laws of sea ice deformation in good agreement with observational scaling laws.

The modified Coulomb rheology is a modification of the elliptic yield curve based on laboratory biaxial compression experiments (Hibler and Schulson, 2000). Introducing friction based failure up to certain compressive load gives the yield curve a teardrop shape. In addition, small tensile stress is allowed to ensure energy dissipation.

The elasto-brittle rheology regards the sea ice as a rigid elastic plate with Hooke's law relating the stress tensor to the strain tensor (Girard et al., 2011). Exceeding the damage threshold decreases the local stiffness. Due to the recalculation of the state equilibrium after each damage event within a time-step, stress redistributes in the ice and damage can propagate in so-called damage avalanches.

2.3   Modeling Sea Ice Dynamics with MITgcm

The MITgcm is a community model for ocean and atmosphere [1]. Losch et al. (2010) introduced its sea ice component that is coupled to the ocean model. In general, the MITgcm sea ice model is based on the viscous-plastic sea ice model (Hibler, 1979) version presented by Zhang and Hibler (1997). The dynamics of sea ice given in the Sections 2.1 and 2.2 are formulated on an Arakawa C grid (Zhang and Hibler (1997) provide a B grid implementation) and can be solved either by line successive over relaxation (LSOR) (Zhang and Hibler, 1997) or by the Jacobian-free Newton-Krylov solver (JFNK) (Losch et al., 2014). Besides the dynamic part, the thermodynamics builds the second main part of the sea ice package, which is based on the surface heat flux computation of Parkinson and Washington (1979) and the snow model of Zhang et al. (1998) (for further description of the thermodynamics please see Losch et al. (2010) and MITgcm Group (2015)).

---

[1]available at (*http://mitgcm.org/*)

Chapter 3

Linear Kinematic Features

Oriented fractures spread in the sea ice covering the Arctic ocean in all seasons. They divide the ice cover in several ice flows and narrow lineaments of open water (Marko and Thomson, 1977; Kwok, 2001; Richter-Menge et al., 2002). These lineaments range from a few meters to basin wide features of hundreds of kilometers (Schulson and Duval, 2009). The fragmentation of ice is caused by stress resulting from relative motion, that is induced by wind stress associated with weather systems, by geometric boundaries such as coastlines or fast ice edge (Richter-Menge et al., 2002), by tides (Holloway and Proshutinsky, 2007), by ocean waves (Squire et al., 1995), or by swell originating from Arctic storms (Asplin et al., 2012). Depending on the processes involved, such as opening, closing and shear (Kwok, 2001), cracks and leads are formed in case of divergence or pressure ridges are formed in case of convergence.

3.1   Observation and Formation

To study the deformation of sea ice, measurements of the ice stress are required. The most direct approach is to deploy stress sensors on the ice cover as done in AIDJEX between 1970 and 1978 or the Surface Heat Budget of the Arctic Ocean (SHEBA) field experiment (Perovich et al., 1999). Besides direct in situ stress measurements, the dispersion of buoys moving with the fractured ice is used to analyze its deformation (Martin and Thorndike, 1985). Nowadays a more powerful tool is

satellite remote sensing providing data of larger regions but with lower temporal and spacial resolution (Kwok, 1998).

Due to the specific localization of the formation process of LKFs, actual observations of this process are rare because of coarse spatial resolution of sensors and buoys as well as the coarse temporal resolution of satellite data. By combining stress sensor data with satellite imagery data, Richter-Menge et al. (2002) showed that LKFs are created under compressive states generated by wind pushing the ice against the coastline. Compressive states are recurrent in the ice (Richter-Menge and Elder, 1998) and LKFs show similarities with laboratory observations of ice under compression (Schulson and Hibler, 1991, 2004). Thus Schulson and Duval (2009) suggested that LKFs form by the wing-crack mechanism illustrated in Fig. 3.1: Dominating compressive states in the ice lead to the deformation of pre-existing linear weaknesses to wing-like cracks. By increasing the load, the ice slides along appropriately oriented weaknesses like thermal cracks (called first cracks) and the stress state changes at the end of the weakness locally from compressive to tensile (Schulson and Hibler, 2004). The concentrated stress at the tips of the weakness initiates secondary cracks called wing cracks, which are oriented in parallel to the maximum principal stress. A sequence of several wing-like cracks combines to a linear fracture as shown in Fig. 3.1.

3.2 Characteristics of LKFs

3.2.1 Shape and Orientation

Given the formation process described above, LKFs exhibit a typical shape of straight leads in the ice interspersed by rhomboidal-shaped openings originating from shear displaced wing cracks. The described shape strongly depends on the forcing on the ice after the formation process, i.e. local divergence will further open the fault whereas local convergence will close the fault again. Furthermore the different directions of motion of single ice floes formed by LKFs (Richter-Menge et al., 2002; Schulson and Duval, 2009) affect the shape of the LKFs, which give LKFs
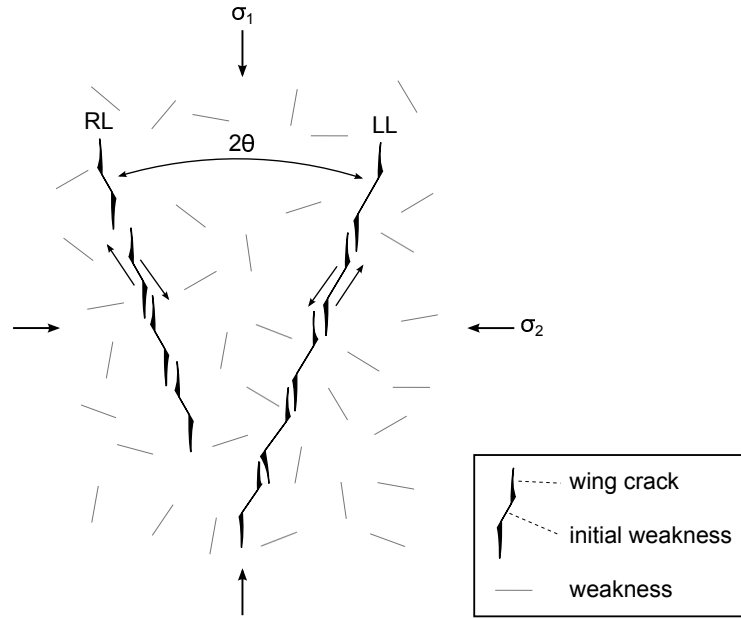
Figure 3.1: Two intersecting faults formed by the wing crack mechanism. The wing cracks form along the direction of the first principal stress σ_1. RL and LL indicating the direction of shear deformation looking from the top across the fault (Schulson and Hibler, 2004).

their typical shape only for a short time after the formation process.

In compression, shear deformation starts at weaknesses oriented with an acute angle of θ to the first principle (compressive) stress σ_1. Depending on the relative shear motion, LKFs are either parallel to each other or intersect each other with an acute angle 2θ, which typically ranges from $2\theta \approx 20°$ to $2\theta \approx 50°$ (Marko and Thomson, 1977; Richter-Menge et al., 2002; Schulson and Duval, 2009). This angle shows huge similarities to laboratory observations and depends on the internal friction coefficient (Schulson and Duval, 2009).

3.2.2 Statistical Properties

The sea ice cover is fragmented into ice floes separated by LKFs. Single ice floes move with approximately uniform velocity. Thus, velocity gradients within the floes are small, whereas floe boundaries are regions of strong velocity gradients inducing high strain rates. Marsan et al. (2004) quantified this localization of strain rates by showing that only 1.6 % of the area accommodate the largest 15 % of the total
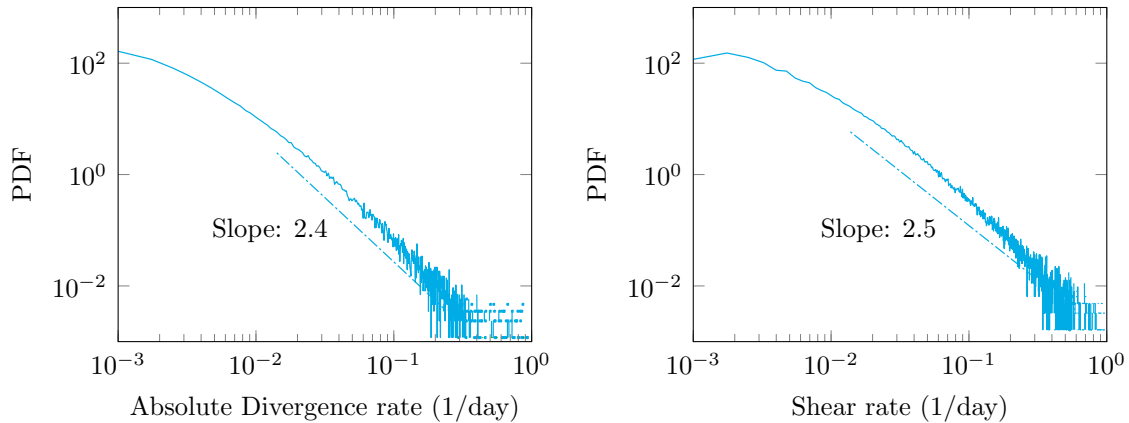
13

Figure 3.2: Probability distribution function (PDF) of absolute divergence and shear derived from RGPS observations for January to March 1997 (Girard et al., 2009)

deformation at a spatial resolution of 20 km for November 6th 1997. Averaging the velocity data over spatial scales of 200 km damps the localization of strain rate events and the area fraction increases to 3.2 %. Using all available data from 1996 to 2005 Stern and Lindsay (2009) obtained comparable values with $\sim 2\,\%$ for 20 km and $\sim 6\,\%$ for 200 km. Girard et al. (2009) determined that 6 % (10 km) and 13 % (100 km) of area accommodate 50 % of shear.

In addition, the *probability distribution function* (PDF)[1] of divergence and shear states illustrates this localization of strain rates. The PDF describes the relative likelihood of certain strain rate events. Girard et al. (2009) presented PDFs for divergence and shear obtained from RGPS velocity data for winter 1997 (Fig. 3.2). The PDFs show a maximum at low strain rates and decreasing probabilities towards large strain rate events. The PDF tends to decrease linearly in log-log-scale,

$$P\left(\dot{\epsilon}\right) \sim \dot{\epsilon}^{-\eta}, \tag{3.1}$$

with a slope that satisfies $\eta = 2.4$ for divergence and $\eta = 2.5$ for shear. With this the distribution fulfills a symmetric Lévy law centered on zero,

$$P\left(x\right) \sim \frac{C}{|x|^{1+\mu}}, \quad \text{for } x \to \pm\infty, \tag{3.2}$$

_____

[1]Strictly speaking we approximate the PDFs by relative frequency distributions as the number of observations is finite.

14

where the exponent $\mu = \eta - 1$ is restricted to $0 < \mu < 2$ and C is a positive constant called scale parameter (Sornette, 2006). Power law distributions following (3.2) are characterized by wild randomness for $\mu < 2$ meaning that extreme values dominate the distribution. These extreme values have major implications on the statistical quantities mean and variance: the variance of power law distributions approaches infinity as the gentle decay at $|x| \rightarrow \infty$ does not lead to an convergence of the integral. In addition for $\mu < 1$, the mean is infinity as the integral diverges as well (Sornette, 2006). For $\mu > 2$, the distribution is in Gaussian attraction and both quantities converge.

The power law tails of the PDFs in Fig. 3.2 reveal that sea ice deformation is dominated by extreme values, and does not follow a Gaussian distribution (Girard et al., 2009). The power law tails exclude also a symmetric exponential distributions indicating turbulent motion as seen for the fluctuating part of sea ice velocity (Rampal et al., 2009). However, the presence of a high amount of large strain events emphasize the localization of strain rates. Finally, Girard et al. (2009) emphasizes a comparison of the complete distribution instead of only comparing its mean and standard deviation, which are insufficient to describe power law distributions in contrast to Gaussian distributions as mentioned above.

3.2.3   Multi Fractal Properties

LKFs spread in sea ice at various scales from a few meters seen in aerial photographs to basin wide scales observed by satellites. Thereby, the patterns of ice floes and LKFs are hardly distinguishable indicating self-similar properties. Mandelbrot (1983) described many phenomena in nature with similar characteristics and called them fractals due to their "fractured" non-integer dimension. Self similar processes are described by power law scaling of the form,

$$M\left(x\right) \sim x^{\alpha}, \tag{3.3}$$

with an observable property M, the scale x and the exponent α coinciding under certain conditions with the fractal dimension (Weiss, 2003). For sea ice, power
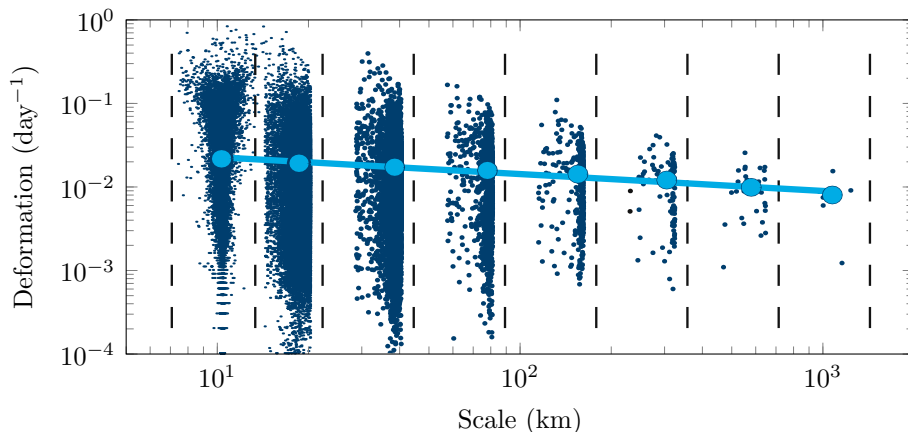
Figure 3.3: Total deformation rate $\dot{\epsilon}(L)$ as function of scale L derived from RGPS data for 6 November 1997 (Marsan et al., 2004). The mean deformation for each scale is indicated by bright blue dots. The line represents the least square fit of the power law (3.4) to the mean deformation values $\langle \dot{\epsilon}(L) \rangle$ with a scaling exponent $H = 0.2$.

law scaling is observed in the floe size distribution (Rothrock and Thorndike, 1984; Lindsay and Rothrock, 1995), in fracture and faulting (Weiss, 2003) and deformation (Marsan et al., 2004; Rampal et al., 2008; Stern and Lindsay, 2009).

Spatial Scaling Laws

As sea ice velocities are needed to estimate deformation two independent data sources are available for scale analysis of sea ice deformation: buoy position data (Rampal et al., 2008; Hutchings et al., 2011, 2012) and feature tracked velocities fields obtained from satellite *synthetic aperture radar* (SAR) images (Marsan et al., 2004; Stern and Lindsay, 2009; Girard et al., 2009). All three presented satellite studies are based on the RADARSAT Geophysical Processor System (RGPS) (Kwok, 1998), which tracks trajectories of 40,000 points with a initial resolution of 10 km.

The approach to deduce scaling laws from both data sets is similar. First the velocity data is averaged over different spatial scales - a process referred to as *coarse graining* - and a tracer for sea ice deformation is derived from those fields for each scale. Most frequently the total deformation rate, given by $\dot{\epsilon} = \sqrt{\dot{\epsilon}_I^2 + \dot{\epsilon}_{II}^2}$ with the divergence and shear rates $\dot{\epsilon}_I$ and $\dot{\epsilon}_{II}$, is used for the scale analysis (Marsan et al., 2004; Stern and Lindsay, 2009; Hutchings et al., 2011, 2012). Next, the mean of all
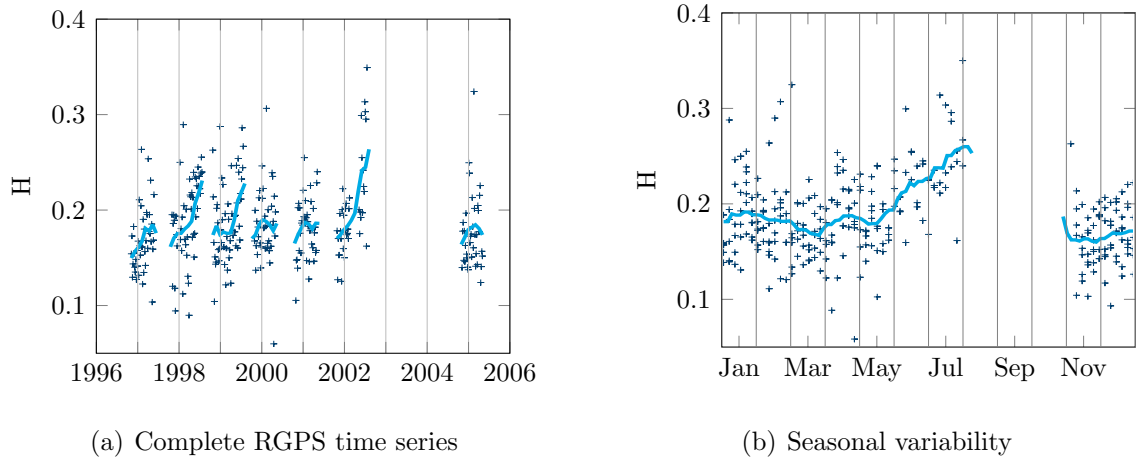
(a) Complete RGPS time series   (b) Seasonal variability

Figure 3.4: Seasonal variability of the scaling law coefficient H for all data (left) and for one year (right). The solid lines represent running means of the scaling law coefficient averaged over 4-month (left) and 1-month (right) (Stern and Lindsay, 2009).

deformation events $\langle \dot{\epsilon}(L) \rangle$ for each scale L is computed. The mean total deformation decreases with increasing spatial scale due to the smoothing of the velocity fields. Fitting the mean deformation to the power law,

$$\langle \dot{\epsilon}(L) \rangle = C\,L^{-H}, \tag{3.4}$$

reveals the spatial scaling law coefficient H (Marsan et al., 2004) and the constant of proportionality representing the mean deformation at scale of 1 km (Stern and Lindsay, 2009). Marsan et al. (2004) obtained a scaling law coefficient of $H = 0.2$, which is in good agreement with 0.18 from Girard et al. (2009) who used the same dataset. In addition, Hutchings et al. (2011) verified this results independently $(H = 0.19)$ with an array of buoys specially deployed for this purpose in the Beaufort Sea in spring 2007.

Stern and Lindsay (2009) analyzed all available RGPS data and reported a seasonal cycle for the scaling coefficient (Fig. 3.4). The scaling coefficient has mean value of 0.18 in wintertime (November to April) and increases to 0.25 in summer (April to August). The thick ice in the wintertime has a high strength. Therefore, stress states are transmitted more likely over long distances through the ice instead of initiating a failure event. Small scale deformation events are thus transmitted to

larger scales as well leading to more similar mean deformation across the scales and a low spatial scaling law coefficient. However, in summertime the thin and loose ice pack is not such a good transmitter of stress. The weaker connection between distant parts causes higher differences in the mean values of deformation and thereby higher scaling law exponents (Stern and Lindsay, 2009). This is consistent with the finding of Stern and Lindsay (2009) that multiyear (MY) ice shows a much smaller scaling exponent ($H = 0.14$, for MY fraction near 1) than first-year (FY) ice ($H = 0.24$, for MY fraction of about 0.2).

Temporal Scaling Laws

Only buoy recorded data is used to deduce temporal scaling laws of sea ice deformation due to the poor temporal resolution of the RGPS data (3 days). Rampal et al. (2008) analyzed buoy trajectories recorded between 1979 and 2002 from the International Arctic Buoy Program (IABP) for temporal scaling. The rate,

$$\dot{D} = \frac{\Delta r}{L\tau},$$ (3.5)

with the separation Δr of two buoys after the time τ, which were initially separated by the distance L, is used as a tracer for sea ice deformation. The standard deviation of this rate $\sigma_{\dot{D}}$ follows a temporal scaling law (Rampal et al., 2008),

$$\sigma_{\dot{D}} \sim \tau^{-\alpha},$$ (3.6)

with the exponent α varying between 0.89 ($L = 1\,\text{km}$, winter) and 0.25 ($L = 300\,\text{km}$, summer) depending on initial separation and season. The exponent is thereby a measure of the degree of intermittency of the deformation process (Rampal et al., 2008), and is bounded by the upper limit $\alpha = 1$ representing single fracturing events at small spatial scales and the lower limit $\alpha = 0$ representing viscous flow at large spatial scales.

Hutchings et al. (2011) found scaling law characteristics for the total deformation rate,

$$\dot{\epsilon} \sim \tau^{-\alpha},$$ (3.7)

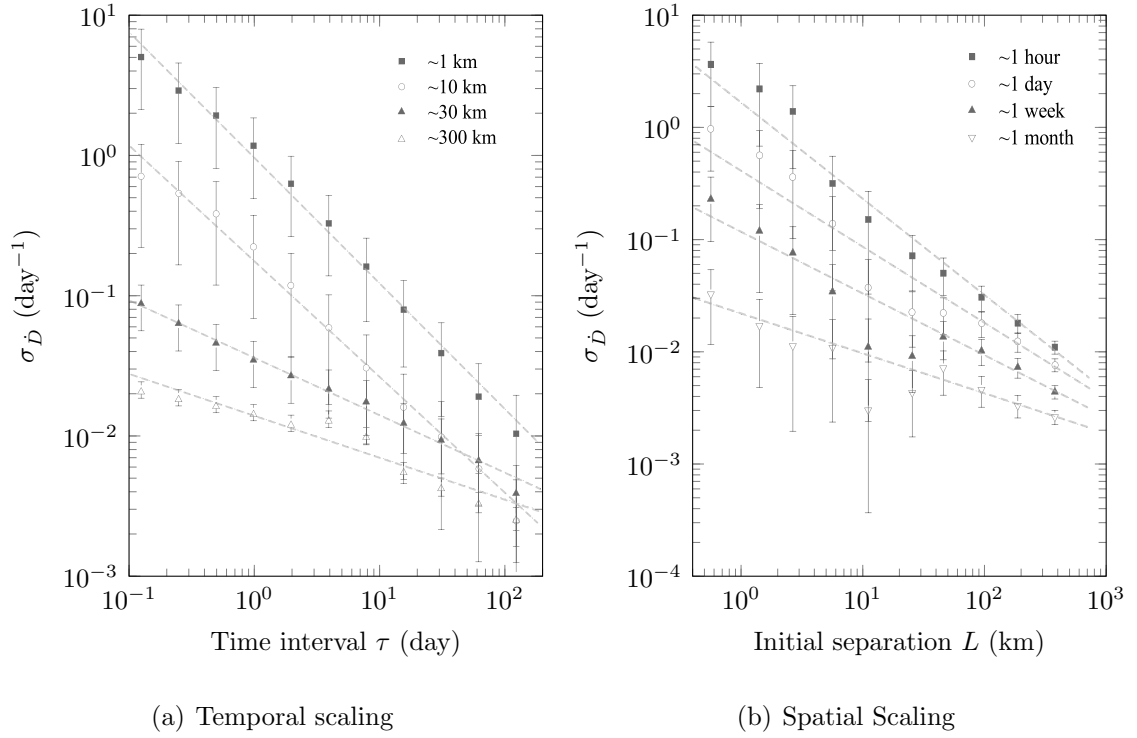(a) Temporal scaling   (b) Spatial Scaling

Figure 3.5: Space time coupling in the scaling characteristics of sea ice deformation for winter (Rampal et al., 2008). (a) Temporal scaling of tracer $\sigma_{\dot{D}}$ depending on the initial separation L. (b) Spatial scaling of tracer $\sigma_{\dot{D}}$ depending on the time interval τ.

derived from the Sea ice Experiment: Dynamic Nature of the Arctic (SEDNA) buoy array. The exponent α approaches 1 for the smallest arrays ($L = 10\,\text{km}$) leading to scaling relationship of the form $\dot{\epsilon} \sim \frac{1}{\tau}$, which characterizes sea ice deformation as a pink noise process (Hutchings et al., 2011).

Space Time Coupling

As indicated already in the section above, Rampal et al. (2008) discovered a coupling between the spatial and temporal scaling that becomes evident in the dependence of the temporal scaling exponent α on the spatial scale L (Fig. 3.5(a)). The spatial scaling of sea ice deformation also dependents on the temporal scales (Fig. 3.5(b)). The dependence becomes apparent in the varying slopes of the scaling laws in Fig. 3.5. The spatial scaling coefficient varies gradually, whereas the temporal scaling coefficient jumps at a threshold for initial separation ($10\,\text{km} < L < 30\,\text{km}$) between the

two extreme values: $\alpha \approx 0.8$ for $L < 10\,\mathrm{km}$ and $\alpha \approx 0.3$ for $L > 30\,\mathrm{km}$.

The temporal scaling of the total deformation rate $\dot{\epsilon}$ depends on the spatial scale as well (Hutchings et al., 2011). This dependence is observed in the spectral analysis of the total deformation rate with a *Fast Fourier Transform* (FFT). At large scales ($L = 140\,\mathrm{km}$) sea ice deformation is described as a red noise process, which is revealed by a linear decrease of the spectral density with a slope of -2. With decreasing scale the spectra are shifted towards white noise and for small scales ($L = 10\,\mathrm{km}$) deformation is approximated by pink noise as the slope is decreased to value of 1.3 (Hutchings et al., 2011).

3.3 Modeling Approaches

Overland and Ukita (2000) and Maslowski and Lipscomb (2003) noted the ability of viscous-plastic sea ice models with high resolution to reproduce LKFs. Since then, Hutchings et al. (2005) and Wang and Wang (2009) modeled LKFs using this approach.

Using the modified Coulomb rheology (Hibler and Schulson, 2000), Hutchings et al. (2005) investigated properties of faults resulting from steady and varying wind forcing in an idealized environment. To insert initial weaknesses in the ice, a randomly distributed ice strength is assumed that sped up the fracturing process. They showed that the number of fractures increases with increasing wind stress as well as inertial oscillations of modeled LKFs. However, Hutchings et al. (2005) did not directly compare the modeled and observed features. Instead they emphasized a comparison based on statistics.

Wang and Wang (2009) compared the LKFs produced with elliptic, modified Coulomb and curved diamond yield curves at different resolutions ($10\,\mathrm{km}$, $5\,\mathrm{km}$ and $2\,\mathrm{km}$,) on a downscaled Arctic Ocean. The simulation time was three days and a reanalysis wind forcing was used. A rough comparison with observational data leads to the result that the curved diamond yield curve is most appropriate for modeling LKFs.

In contrast to the isotropic models used in Hutchings et al. (2005) and Wang and Wang (2009), Hibler (2001) used an anisotropic sea ice model coming to the conclusion that qualitative differences to an isotropic modified Coulomb rheology is small.

3.4   Predictability of LKFs

The decline of Arctic sea ice associated with the growing economic interest in polar regions increases the demand for a reliable forecast of sea ice. Current *global climate models* (GCM) show predictive skill regarding sea ice anomalies on seasonal and interannual time scales (Koenigk and Mikolajewicz, 2009; Blanchard-Wrigglesworth et al., 2011; Holland et al., 2011; Tietsche et al., 2014). Recent developments on sea ice forecast systems seem promising and provide a skillful prediction of the sea ice extent on seasonal time scales (Chevallier et al., 2013; Sigmond et al., 2013; Wang et al., 2013). However all these forecasts and predictability studies focus on pan Arctic quantities such as sea ice extent and thickness. Processes of regional scale like LKFs have not been object of predictability studies so far.

Solely Hutchings et al. (2005) supposes a low predictability of modeled LKFs due to the strong dependence of failure zones on the wind stress. Uncertainties in wind forcing data and model biases could result in systematic differences of modeled LKFs compared to observations. Instead of direct comparison Hutchings et al. (2005) emphasizes a statistical comparison between modeled and observational LKFs.

Chapter 4

Experimental Set-Up

An idealized environment is chosen as experimental set-up for computing limits at high resolution. The same experimental set-up is used for several model runs with gradually refined resolutions from $10\,\mathrm{km}$ up to $1\,\mathrm{km}$ to investigate the influence of the resolution on the resulting viscous-plastic sea ice models.

The idealized environment has a quadratical shape and a size of $500\,\mathrm{km}$ by $500\,\mathrm{km}$ surrounded by closed boundaries. The ocean in this area has a uniform depth of $100\,\mathrm{m}$ and is at rest. Fig. 4.1 illustrates this configuration.

4.1   Initial Conditions

Initially, the ocean is completely covered with ice and, hence, the sea ice concentration is $100\,\%$ in all grid cells. The ice is at rest at the beginning of the simulation and there is not any snow on top of the ice. The time scales of thermodynamic processes in the ice are large compared to dynamic processes. Thus, thermodynamic processes can be neglected in this study. Neither growth or melt of ice due to thermodynamics nor snowfall is considered.

Hutchings et al. (2005) used randomly varying initial ice strength to induce initial weaknesses in the ice and to model LKFs. Here, two different configurations are used to determine the influence of initial weaknesses: The first configuration assumes an uniform thickness of the sea ice. As the parametrization for ice strength (2.12)
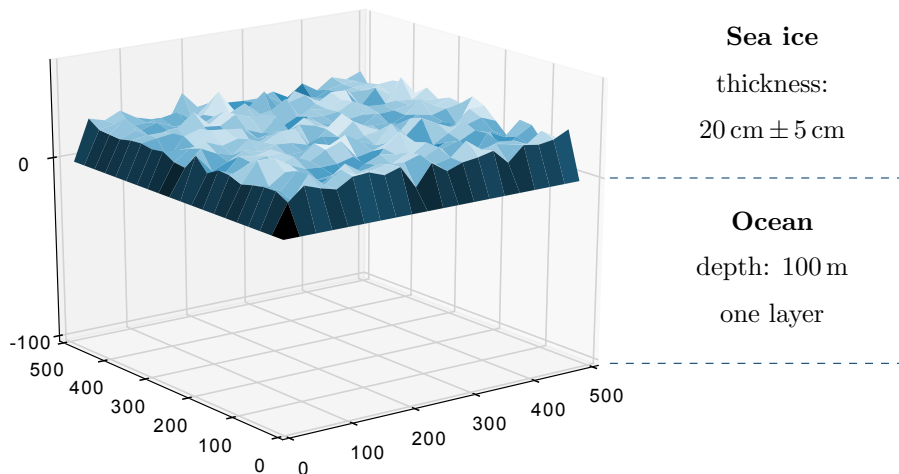
Figure 4.1: Sketch of the experimental set-up: ocean basin (500 km by 500 km) covered by sea ice with random thickness distribution (mean: 20 cm, standard deviation: 5 cm).

is a function of sea ice concentration and thickness, the ice strength is uniform in this configuration. In the second configuration the thickness of the sea ice is randomly distributed resulting in an analogously random distribution of ice strength. According to Hutchings et al. (2005), this kind of ice strength distribution represents initial weaknesses in the ice cover, acting as seeds of the fracturing process. The thickness of the sea ice follows a Gaussian distribution with a mean of 20 cm and a standard deviation of 5 cm. The thickness distributions for different resolutions of the spatial model are obtained by coarse graining the high resolution (1 km) field. The perturbations are spatially correlated with a scale of 10 km to ensure that the distributions have a similar mean and standard deviation across different spatial resolutions.

4.2 Wind Forcing

The model is driven by three different types of wind forcing. The first set of experiments is performed with an idealized wind forcing, whereas for subsequent experiments reanalysis wind forcings with different underlying spatial resolution are used.

24

4.2.1 Idealized Wind Forcing

The idealized wind forcing represents a sequence of passing weather systems lasting 16 days altogether. First, a low pressure system moves from southwest to northeast (cf. Fig. 4.2(a)) followed by a high pressure system moving in the opposite direction (Fig. 4.2(b)). The pressure fields are determined assuming associated length scales of 900 km for low pressure system and 1200 km for high pressure system as well as a pressure anomaly of 20 mbar. The wind field is calculated from the pressure fields by the geostrophic wind approximation with an additional friction term characterizing the wind in the mixed boundary layer (Holton and Hakim, 2012):

$$C_d \left| \mathbf{U_a} \right| \mathbf{U_a} + f \, \mathbf{k} \times \mathbf{U_a} + \frac{1}{\rho_a} \nabla p = 0, \tag{4.1}$$

where C_d is the surface drag coefficient. The nonlinear equation (4.1) is solved on each grid point with an accuracy of 10^{-4} m/s. The friction term added to the geostrophic wind generates converging wind fields for low pressure systems and diverging wind fields for high pressure systems, see Fig. 4.2. Compared to geostrophic winds used by Hutchings et al. (2005), converging and diverging wind fields induce higher internal stress in the ice and, therefore, are thought to induce stronger sea ice deformation.

4.2.2 Reanalysis Wind Forcing

In a different set of experiments, the model is forced with two different reanalysis wind products to achieve more realistic wind conditions. To this end, a 500 km by 500 km region north of Svalbard is selected in wind products for the year 2009. The box is centered around 84° N, 20° W and shown in Fig. 4.3. The surface winds of the Japanese 25-year Reanalysis (JRA-25) and of the Atmospheric Model high resolution 10-day forecast (HRES) provided by European Centre for Medium-Range Weather Forecasts (ECMWF) are interpolated on the model grid. The two datasets mainly differ in the spatial resolution.

In contrast to the idealized forcing, the reanalysis wind forcing is not symmetric. The randomized paths of weather systems are subject to a general circulation. To

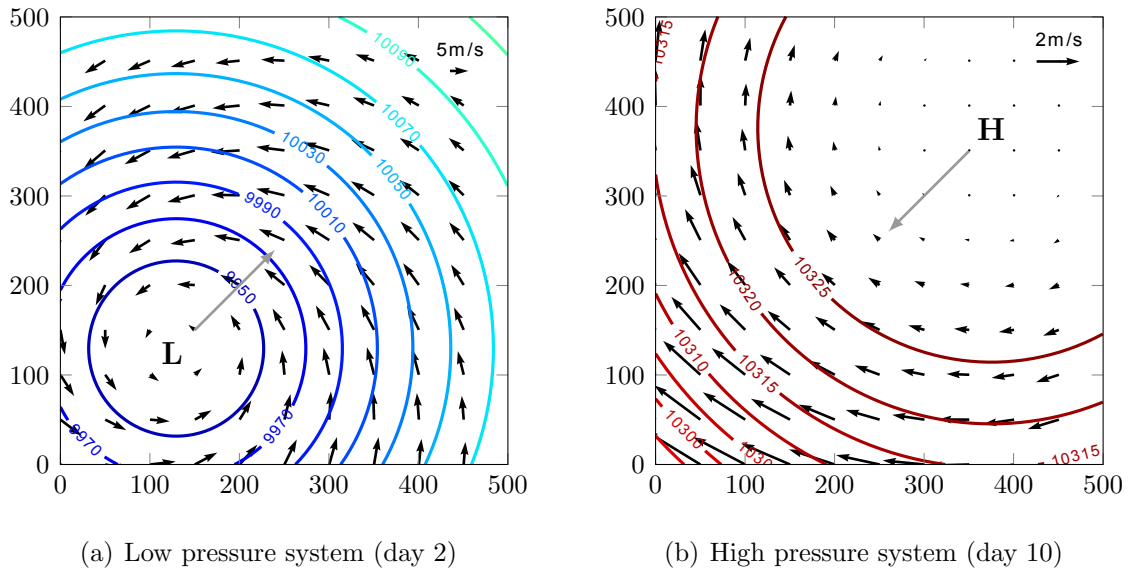(a) Low pressure system (day 2) (b) High pressure system (day 10)

Figure 4.2: Idealized wind forcing composed of a sequence of a low and a high pressure system. The pressure fields are given in contour lines. Black arrows indicate the wind velocity. The center of the pressure systems are marked with L for low and H for high, respectively. Gray arrows show the path of the pressure systems.

account for this effect and to prevent the ice from being pushed to one corner, the mean wind field is subtracted from the wind forcing. However, the mean wind field can be only determined imprecisely because of the variability of its spatial and temporal scales.

JRA-25 Reanalysis

The JRA-25 Reanalysis data set (Onogi et al., 2007) covers the period from 1979 to 2004 and is followed up by the Japan Meteorological Agency (JMA) Climate Data Assimilation System (JCDAS) providing real-time data with the same system. The global model has a spatial resolution of around 120 km (Onogi et al., 2007). The surface (10 m) zonal and meridional wind from this data set are used.

ECMWF High Resolution Forecast

To refine the spatial resolution of the wind forcing, ECMWF's HRES data set is used providing a spatial resolution of 0.125° corresponding to 14 km. It is the global
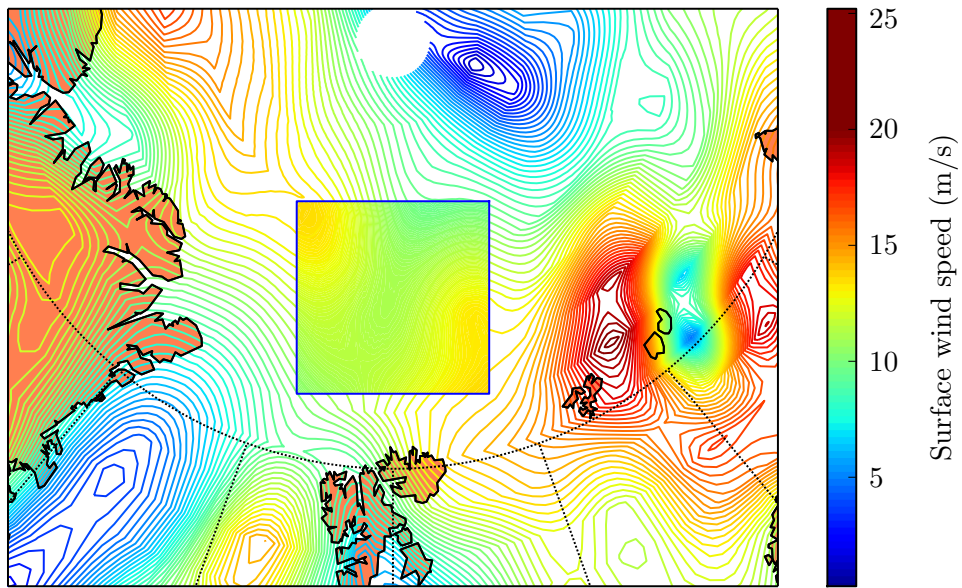
Figure 4.3: JRA-25 surface wind speed for January 13th, 2009 given in contour lines. The region of interest is marked by the blue box and the interpolated wind forcing is presented as a contour plot inside the box.

wind product with the highest available spatial resolution and again the 10 m surface winds are used.

Chapter 5

Experiments with Idealized Wind Forcing

The experiments with idealized wind forcing described in Section 4.2.1 are the first experiments performed to study the behavior of the MITgcm sea ice component at high resolution. In this study, the resolutions used for long term experiments are 10 km, 5 km, 2 km and 1 km, although for short experiments intermediate resolutions are implemented as well. The model runs assuming two types of initial condition, a uniform sea ice thickness and randomly distributed thickness, to study the influence of initial weaknesses in the ice to the fracture process. The time span of the long term experiments is 256 days corresponding to 8 passages of the idealized low and high pressure systems.

5.1 Modeled LKFs

In all results of the long term experiments, LKFs are observed independently of the given resolution. Day 23 is arbitrarily picked to present some results of these model runs: Fig. 5.1 presents the sea ice concentration A, Fig. 5.2 the mean ice thickness, and Fig. 5.3 the shear deformation. All three figures show the deformation of the sea ice by the passing weather systems inside the closed boundaries. Thereby, the amount of LKFs observed is increasing with the resolution, whereas the regions
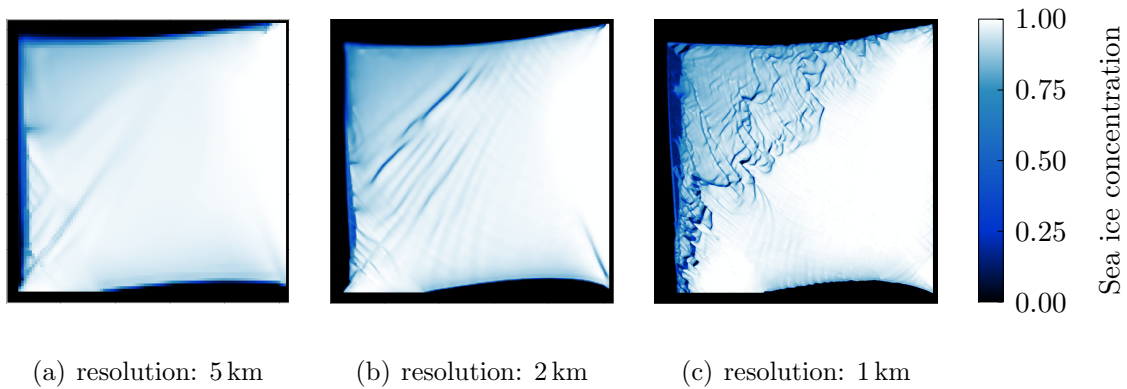
(a) resolution: 5 km   (b) resolution: 2 km   (c) resolution: 1 km

Figure 5.1: Modeled sea ice concentration A after 23 days simulation (shortly after second passage of the low pressure system).

(a) resolution: 5 km   (b) resolution: 2 km   (c) resolution: 1 km
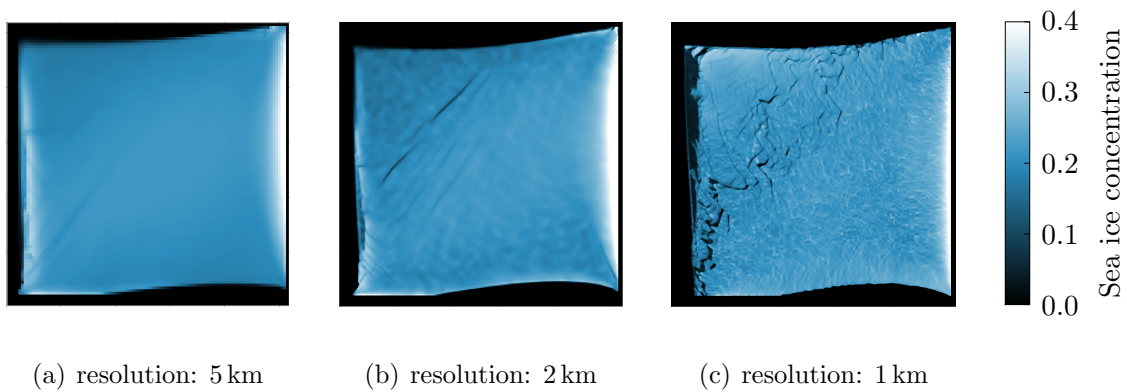
Figure 5.2: Modeled sea ice thickness h averaged over grid cell after 23 days simulation (shortly after second passage of the low pressure system).
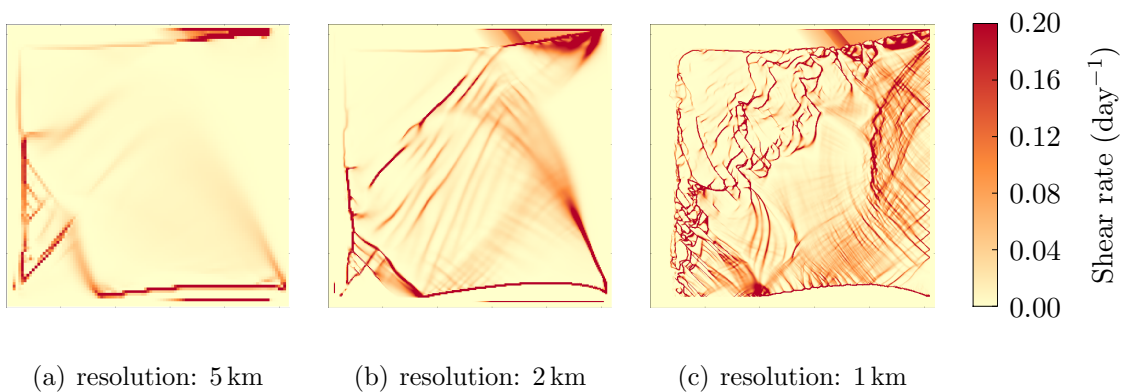

(a) resolution: 5 km   (b) resolution: 2 km   (c) resolution: 1 km

Figure 5.3: Modeled shear deformation ϵ_{II} after 23 days simulation (shortly after second passage of the low pressure system).

in which LKFs concentrate are conserved: a cohesive ice pack is located in the east, whereas the northwest corner exhibits lower sea ice concentration. LKFs are mainly located along the diagonal corresponding to the path of the pressure systems. Towards the northwest, the density of LKFs along the diagonal increases, because the ice strength is lower due to the lower sea ice concentration.

In the 5 km and 2 km run, (a) and (b) in Fig. 5.1,5.2 and 5.3, the main direction of leads is parallel to the diagonal. Smaller leads are found perpendicular to this direction. In a 1 km resolution (c), this direction is dominant and there are fewer LKFs parallel to the diagonal. However, the northwest corner with the low sea ice concentration is separated by a region of ragged leads spreading along the direction of path of weather systems. For the coarser resolutions, this region of low sea ice concentration is separated from the dense ice pack with distinct leads oriented in parallel to the diagonal. The massive increase in density and the details of LKFs at 1 km resolution as well as its more chaotic appearance suggest a change in regime. Some of theses differences might be caused by the different onset of ice motion in different resolutions. The 2 km and 5 km start moving with the first passage of the low pressure system, whereas for the 1 km sea ice motion sets in with the approaching high pressure system. This phenomena will be described in more detail in Section 5.2. Another reason might be a higher sensitivity to the initial perturbations in sea ice thickness in the 1 km run. In addition the increasing number of degrees of freedom permits a progressive chaotic behavior.

Analyzing the sea ice concentration (Fig. 5.1), the thickness (Fig. 5.2) and the shear rate (Fig. 5.3), larger LKFs can be identified in all of them, whereas smaller LKFs are best visible in the shear rate and the concentration but not always in the thickness. LKFs are easily detected in the shear rate, as strain rates are concentrated along LKFs.
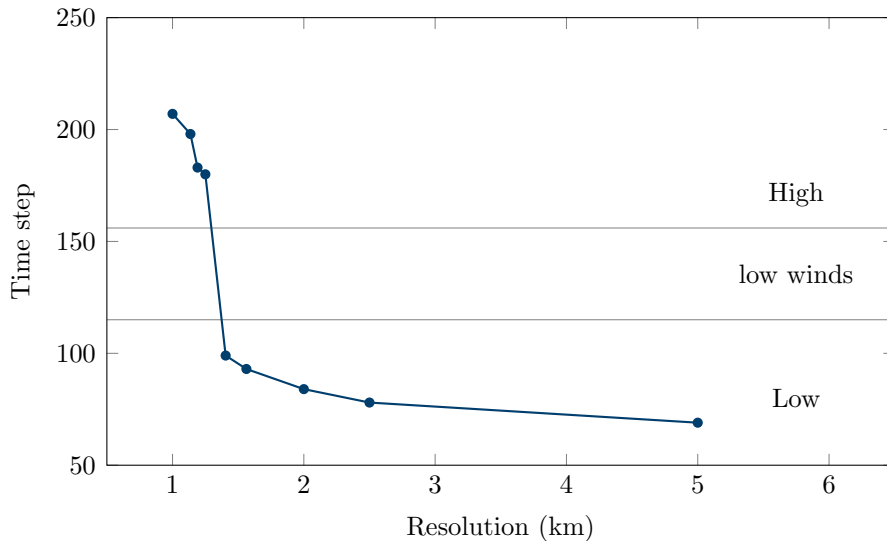
Figure 5.4: Resolution dependent break-up point of the sea ice for randomly disturbed initial sea ice thickness (mean: 20 cm, standard deviation: 5 cm). The time step of the model is 1 hour. The different parts of the wind forcing are denoted by *low* for low pressure system, *high* for high pressure system, and *low winds* for the intermediate part of changing weather systems, which is characterized by low winds.

5.2 Break Up Time of Sea Ice

As mentioned above the time, when the ice separates from the boundaries, increases with refining the resolution. To analyze this relation, short experiments (200 h to 400 h) were carried out at various resolutions of the model (1 km, 1.19 km, 1.25 km, 1.4 km, 1.56 km, 2 km, 2.5 km, 5 km).

Although small viscous creep occurs before the onset of ice motion, the ice velocities increase drastically at this onset. The abrupt separation of the sea ice from the boundary induces a high acceleration of sea ice. Therefore, the time step is detected easily by determining the maximum velocity gradient. This time step is called a break up point in the following and is presented for different resolutions in Fig. 5.4. The delay of the break up point with increasing resolution becomes apparent in Fig. 5.4, especially the sudden increase between 1.4 km and 1.25 km is striking. However, the underlying wind forcing explains this long delay, as after the break up point at 1.4 km resolution the low pressure system leaves the region and the area is exposed to low winds due to the transition of the weather systems. The
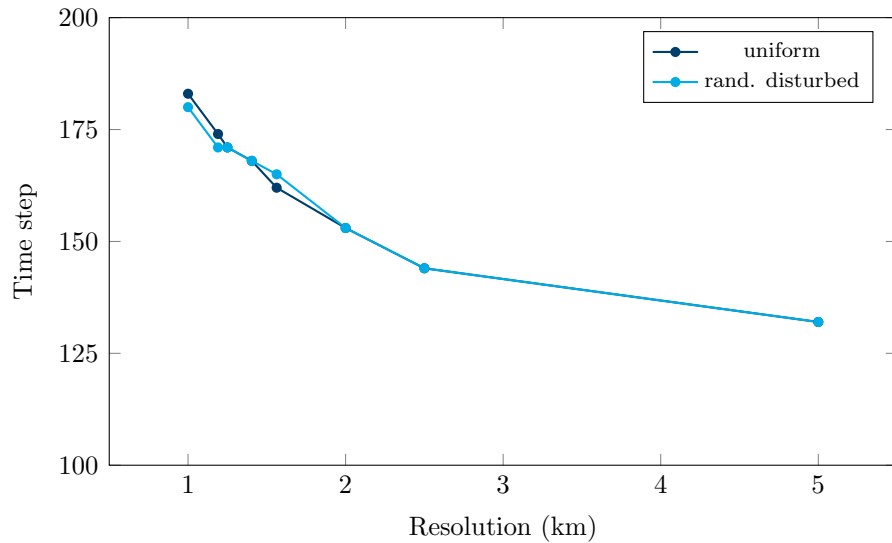
Figure 5.5: Resolution dependent break-up point of the sea ice for different initial conditions: uniform sea ice thickness (20 cm) and randomly disturbed sea ice thickness (mean: 20 cm, standard deviation: 5 cm).

low winds induce less stress in the sea ice to initiate a plastic deformation. The wind speed increases with the approaching high pressure system and the sea ice breaks up.

5.2.1 Wind Forcing Dependence

A second short experiment is performed using a stretched forcing[1] to obtain a break up for all resolutions inside the passing low pressure systems. In addition, two different initial conditions for sea ice thickness (uniform and randomly distributed) are implemented to study whether initial weaknesses in the ice induce a faster break up.

An ice motion sets in during the passage of the low pressure system for all resolutions in this experiment, as seen in Fig. 5.5. Both curves suggest an exponential increase of the break up point with resolution. In contrast to Hutchings et al. (2005), the influence of the initial conditions seems to be negligible as there are only small variations for high resolutions.

---

[1]The pressure systems of the idealized forcing move half as fast. Hence, the passage of the low pressure system lasts 16 days.

5.2.2 Ice Strength Dependence

The break-up point marks the sudden transition from viscous deformation to plastic deformation. A later break up point for refined resolution indicates that more viscous deformation takes place in the high resolution runs compared to a lower resolution. For a low resolution plastic deformation is dominant, which coincides with the observation that the low resolution sea ice appears to be stiffer than the high resolution results. This observation is in good agreement with Bouchat and Tremblay (2014) showing that the frictional dissipation due to plastic deformation decreases with refining resolution. To account for this effect, Bouchat and Tremblay (2014) suggests an increase of the ice strength in isotropic compression P^*. In contrast, Overland and Pease (1988) suggested to decrease P^* with increasing resolution, as the internal stress terms need to balance terms in the momentum balance (2.1), which scale with $P^*/\Delta x$. Our results support this suggestion.

For the highest resolution run (1 km), several short term experiments with varying P^* were performed to study the sensitivity of the break-up point to P^*. The second objective of these experiments is to find a suitable P^* in order to achieve the same break up point for the 1 km and 2.5 km resolution. Decreasing the ice strength under isotropic compression for the 1 km resolution to $P^* = 1.4 \cdot 10^4\, Nm^{-1}$, the modeled sea ice separates from the boundaries at the same time step for both resolutions. The time series of sea ice concentration is presented in Fig. 5.6.

Fig. 5.6 shows the better agreement in the shape and movement of the two ice covers compared to Fig. 5.1. The break-up point for both resolution is at time step 26 (26 hours). The main features coincide for both resolutions: the orientation of LKFs (parallel to the path of the pressure systems: (k) and (o), (l) and (p); in the north east corner: (i) and (m), (j) and (n); in the south east corner: (d)) and areas of low sea ice concentration (eastern edge of the ice cover: (d) and (h), (l) and (p); western edge of the ice cover: (j) and (n); north west corner: (i) and (m)). However the difference in behavior described in Section 5.1 between both runs remains, as the details and density of LKFs in the 1 km run are higher compared to the 2.5 km run.
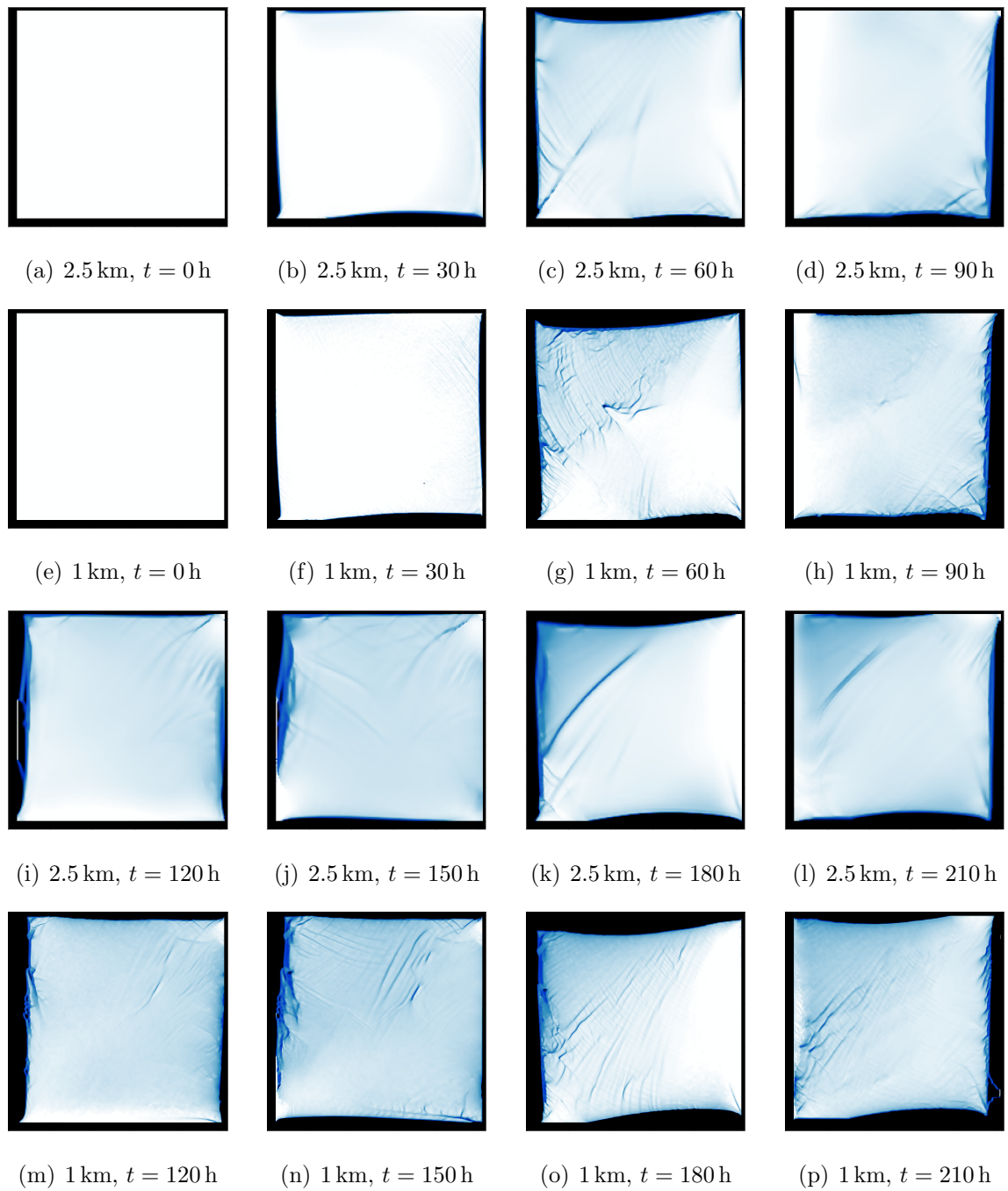
(a) 2.5 km, $t = 0$ h   (b) 2.5 km, $t = 30$ h   (c) 2.5 km, $t = 60$ h   (d) 2.5 km, $t = 90$ h

(e) 1 km, $t = 0$ h   (f) 1 km, $t = 30$ h   (g) 1 km, $t = 60$ h   (h) 1 km, $t = 90$ h

(i) 2.5 km, $t = 120$ h   (j) 2.5 km, $t = 150$ h   (k) 2.5 km, $t = 180$ h   (l) 2.5 km, $t = 210$ h

(m) 1 km, $t = 120$ h   (n) 1 km, $t = 150$ h   (o) 1 km, $t = 180$ h   (p) 1 km, $t = 210$ h

Figure 5.6: Time series of modeled sea ice concentration A for adapted ice strength under isotropic compression P^* for 1 km resolution to achieve the same break up point as 2.5 km resolution (1 km: $P^* = 1.4 \cdot 10^4 \, Nm^{-1}$ and 2.5 km: $P^* = 2.678 \cdot 10^4 \, Nm^{-1}$). The same colorbar as in Fig. 5.1 is used.
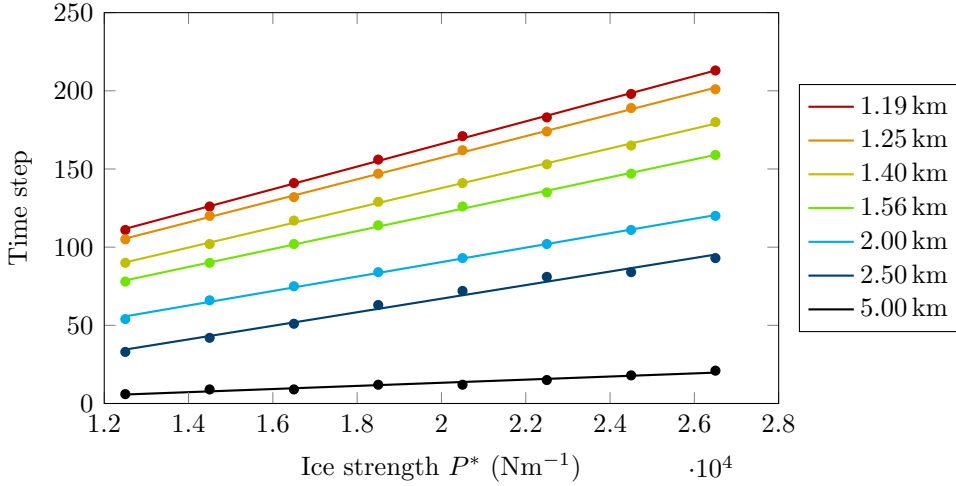
Figure 5.7: Break up time as a function of the ice strength for different resolutions indicated by different colors. The break-up time steps are linearly increasing with the ice strength.

Break-up point function of resolution and ice strength?

This result encouraged further studies of the relationship between resolution, ice strength and break up point. Short experiments with varying P^* were performed for a broad range of resolutions. To definitely exclude the influence of the wind forcing, a steady wind field is used, which corresponds to the presence of a low pressure system. The break-up point is determined by a function of ice strength for each resolution, and is presented in Fig. 5.7.

The break-up point t_b is a linear function of the ice strength P^* for a constant resolution Δx,

$$t_b \left(P^*, \Delta x = const \right) = a \left(\Delta x \right) \cdot P^* + b \left(\Delta x \right). \tag{5.1}$$

Fig. 5.7 shows an increase of the slope $a \left(\Delta x \right)$ with decreasing resolution. To obtain the complete function $t_b \left(P^*, \Delta x \right)$, the resolution dependence of the coefficients $a \left(\Delta x \right)$ and $b \left(\Delta x \right)$ has to be determined. The coefficients $a \left(\Delta x \right)$ and $b \left(\Delta x \right)$ as a function of the resolution Δx are plotted in Fig. 5.8. The coefficients decrease with increasing resolution except for $b \left(\Delta x = 5 \, km \right)$, which is larger than $b \left(\Delta x = 2.5 \, km \right)$. Since Fig. 5.8 does not indicate an obvious choice of fitting function, the Ansatz for the fitting function has to be constraint by other considerations. First of all it is assumed, that with increasing resolution the slope $a \left(\Delta x \right)$ decreases and is limited
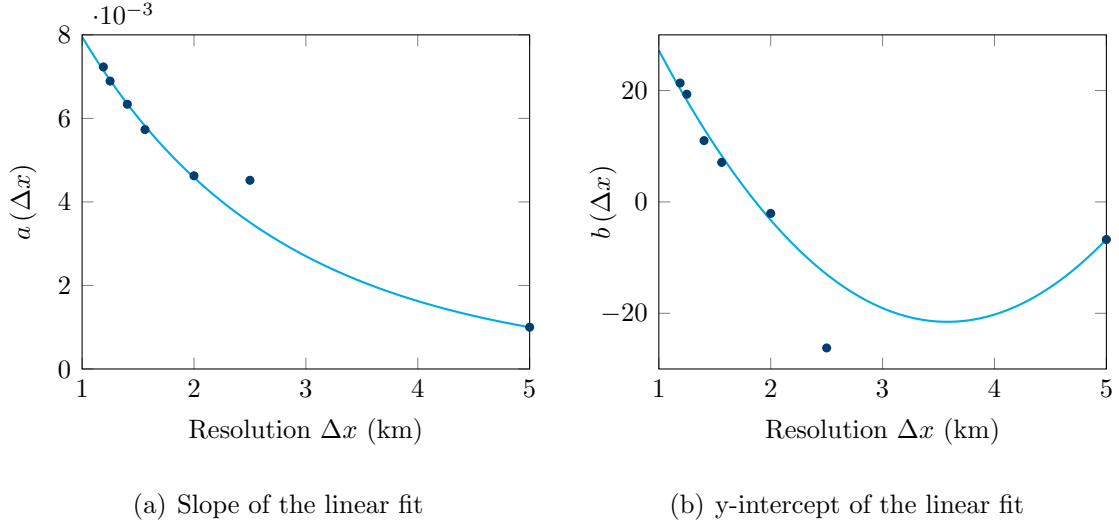
(a) Slope of the linear fit   (b) y-intercept of the linear fit

Figure 5.8: Resolution dependence of the coefficients $a\left(\Delta x\right)$ and $b\left(\Delta x\right)$ of the linear relationship (5.1). The coefficients for the 2.5 km run are an outlier and therefore neglected in the least square fits presented in pale blue.

by zero to ensure that a higher ice strength leads to a later break up point,

$$\frac{d\,a\left(\Delta x\right)}{d\,\Delta x} < 0, \tag{5.2}$$

$$\lim_{\Delta x \to \infty} a\left(\Delta x\right) \to 0. \tag{5.3}$$

Taking these two constraints (5.2) and (5.3) and the distribution of the known values of the slope (Fig. 5.8(a)) into account, a exponential function is chosen for the slope $a\left(\Delta x\right)$,

$$a\left(\Delta x\right) = e^{\alpha\cdot\Delta x+\beta}. \tag{5.4}$$

There are no further constraints for the intercept $b\left(\Delta x\right)$, as this parameter strongly depends on the forcing used. We choose a second order polynomial to estimate the intercept $b\left(\Delta x\right)$,

$$b\left(\Delta x\right) = \gamma\Delta x^2 + \delta\Delta x + \epsilon. \tag{5.5}$$

The unknown coefficients α, β, γ, δ, and ϵ are determined by a least square fit to the model results[2]. The obtained results are given in Tab. 5.1. Hence the final function

---

[2]Resolution 2.5 km is neglected as an outlier in this estimate.

Table 5.1: Coefficients determined with a least square fit of the coefficient functions to the model results of break up points.

α	β	γ	δ	ϵ
$-5.147 \cdot 10^{-4}$	-4.338	$7.333 \cdot 10^{-6}$	$-5.248 \cdot 10^{-2}$	72.369

of the break up time is,

$$t_b \left(P^*, \Delta x\right) = P^* e^{\alpha \cdot \Delta x + \beta} + \gamma \Delta x^2 + \delta \Delta x + \epsilon \tag{5.6}$$

A comparison between the fitted break-up time and the time observed in the results of the model is presented in Fig. 5.9. Overall the suggested function (5.6) agrees well with the modeled break-up time, and can be used to determine the ice strength P_1^* in a high resolution model Δx_1 in such a way, that ice breaks up at the same time step as in a model run with given ice strength P_2^* and model resolution Δx_2,

$$P_1^* = P_2^* \, e^{\alpha(\Delta x_2 - \Delta x_1)} + e^{-\alpha \Delta x_1 - \beta} \left[\gamma \left(\Delta x_2^2 - \Delta x_1^2\right) + \delta \left(\Delta x_2 - \Delta x_1\right)\right]. \tag{5.7}$$

Fig. 5.6 indicates that a synchronous break-up of the ice for different resolutions results in more comparable sea ice extents. Hence, the break-up point seems to be one tracer for the dynamic behavior of the modeled sea ice. Using (5.7) to adjust the break up point makes a better comparison between model runs of different resolutions possible. However, (5.7) is insufficient to determine P^* in case of the time varying idealized forcing (cf. Appendix B). For this configuration a new relationship (5.1) is determined, emphasizing a strong dependence of this relation on the wind forcing.

5.3 Statistical Properties of Modeled Sea Ice

The idealized environment inhibits direct comparison of modeled LKFs with observations made in the field. Therefore, another form of comparison is needed. In the following model, results are compared with observational data by means of statistical quantities.
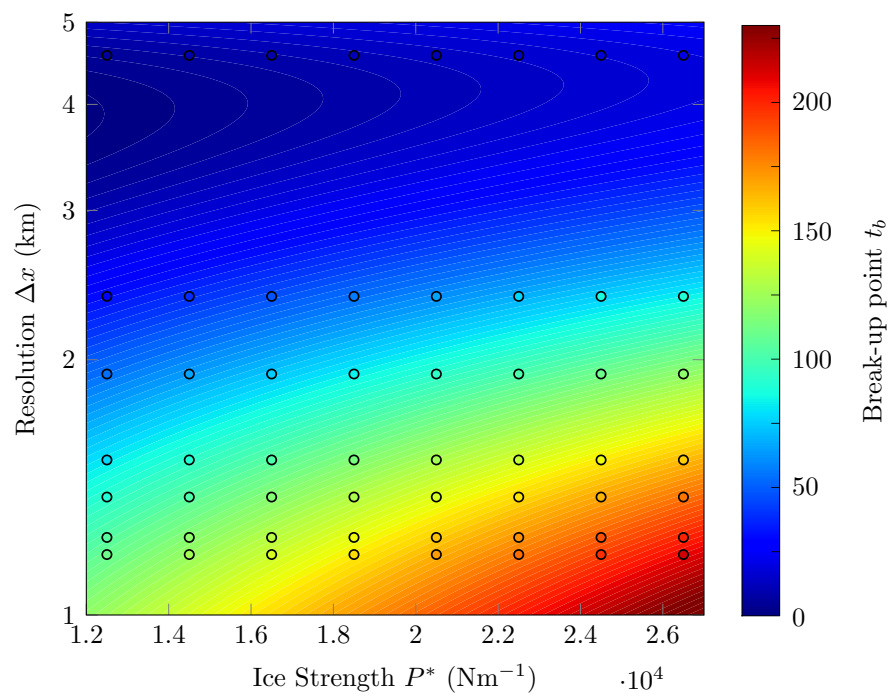
Figure 5.9: Comparison of fitted break up time as contour plot and observed break up time in model results as points. Configurations of resolution Δx and ice strength P^* lay on the same contour line shown in equal colors.
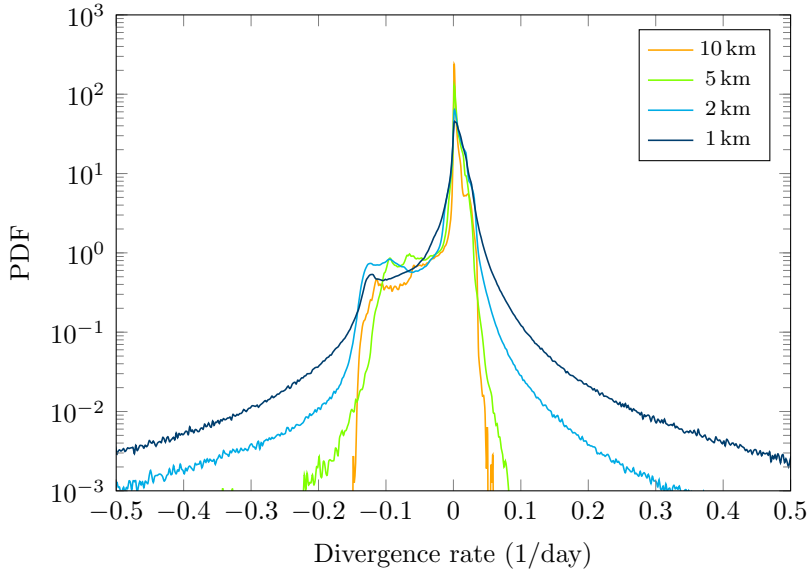
Figure 5.10: PDF of absolute divergence rate ϵ_I for different resolution.

5.3.1 Probability Distributions of Sea Ice Deformation

Fig. 5.10 and 5.11 shows the probability distributions of divergence rate, the absolute divergence rate and the shear rate obtained from long-term experiments for the different model resolutions. Due to limits in the computation, only the first 83 days of the 1 km run are analyzed, for the other resolutions all 256 days are considered. All grid points closer than 100 km to the boundary are excluded from the analysis to filter the effect of boundaries, and a spin-up time of 100 h is assumed. The data is filtered for sea ice concentration values lower than 0.2^3 to exclude open water areas from the analysis. The PDF is approximated by normalized histogram with 1000 bins.

The PDFs in Fig. 5.10 are clearly asymmetric with highest probabilities for low converging states and higher probabilities for mid-size diverging states ($\sim 0.15 \, \mathrm{day}^{-1}$). The mean and standard deviations of divergent and shear rate are given in Tab. 5.2. For all resolutions the mean is slightly positive. The standard deviation increases with refining resolution, because the probability of high strain rate events is higher. This increasing probability leads to a flattening of the tails of the PDFs. For the 10 km run, strain rates are limited by an absolute value of $\sim 0.15 \, \mathrm{day}^{-1}$, whereas

---

[3]Higher thresholds were also tested leading to similar PDFs of strain rates.
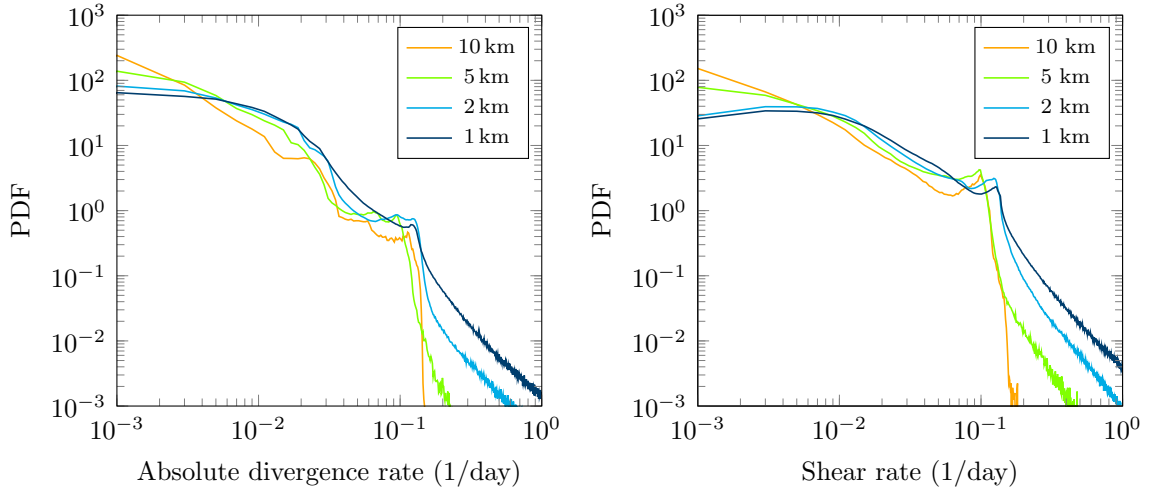
Figure 5.11: PDFs of absolute divergence rate $|\epsilon_I|$ and shear rate ϵ_{II} for different resolutions.

at 1 km resolution larger strain rate events occur quite frequently. As introduced in Section 3.2.2, the slope of the power law tails is determined in the log-log-scale plots (Fig. 5.11(a) and 5.11) to quantify this flattening. The slope is computed with a least square fit of (3.1) to the linear decreasing part of the PDFs in the interval $0.1\,\mathrm{day}^{-1}$ to $1\,\mathrm{day}^{-1}$ and are presented in Tab. 5.2.

The slope decreases drastically with refining resolution. It reaches a minimum of 2.2 for the absolute divergence rate and 2.4 for the shear rate at 1 km model resolution. In contrast, the slopes are considerably larger (26.6 for the absolute divergence rate and 13.1 for the shear rate) for the coarsest resolution of 10 km, and presumably mark a cut-off of higher strain rate events. At this resolution, the PDF is in Gaussian attraction as $\mu > 2$, and the sides of the distributions approach the Gaussian distribution in Fig. 5.12. The distribution of the high resolution run shows power law tails ($\mu = 1.2,\ 1.4$) and thus differs clearly from the Gaussian distribution with the same mean and standard deviation. Slopes of the power law tails of $\eta \leq 3$ characterize distributions with wild randomness, which are dominated by extreme values (Sornette, 2006). Observational slope values at scales from 10 km to 20 km are 2.4 for absolute divergence rate (Girard et al., 2009), 2.5 for shear rate (Girard et al., 2009) and 2.5 for total deformation (Girard et al., 2009). The model results approach this values as the model resolution decreases, and for the 1 km resolution

41

Table 5.2: Mean and standard deviation (std) of divergence, shear rate, and ice strength for long term model runs with idealized wind forcing.

Resolution		1 km	2 km	5 km	10 km
	mean (day^{-1})	$2.91 \cdot 10^{-3}$	$4.23 \cdot 10^{-4}$	$2.59 \cdot 10^{-4}$	$7.57 \cdot 10^{-4}$
$\dot{\epsilon}_{\mathrm{I}}$	std (day^{-1})	0.110	0.041	0.021	0.019
	Slope η	2.195	2.386	8.881	26.620
	mean (day^{-1})	0.043	0.034	0.026	0.020
$\dot{\epsilon}_{\mathrm{II}}$	std (day^{-1})	0.128	0.054	0.034	0.030
	Slope η	2.373	2.624	3.346	13.144
Ice speed	mean (m/s)	$5.68 \cdot 10^{-7}$	$4.50 \cdot 10^{-7}$	$3.51 \cdot 10^{-7}$	$2.61 \cdot 10^{-7}$
	std (m/s)	$1.92 \cdot 10^{-6}$	$7.39 \cdot 10^{-7}$	$4.26 \cdot 10^{-7}$	$3.94 \cdot 10^{-7}$
Number of observations		$3.29 \cdot 10^{7}$	$3.87 \cdot 10^{7}$	$6.28 \cdot 10^{6}$	$1.57 \cdot 10^{6}$

the slopes fall below the observational values. However, Marsan et al. (2004) stated a decreasing slope with increasing resolution due to the scaling nature of strain rate fields. Hence, the slopes are expected to be lower at scales of 1 km compared to the observational values at 10 km.

Wind Forcing Dependence

However, the PDFs are contaminated by several peaks making a least square fit over a broader interval impossible. From a smooth curve more accurate slopes are deduced and therefore the origin of the peaks is of interest. The two major deviations from a symmetric shape are found at $\sim -0.15\,\mathrm{day}^{-1}$ and $\sim 0.025\,\mathrm{day}^{-1}$. One distinct peak in the converging and diverging domain each, point the wind forcing as a possible cause.

The PDF of the wind stress τ_a was analyzed to investigate the influence of wind forcing on the modeled strain rates. The wind stress is computed by (2.2) and the resulting time series is sliced in several intervals corresponding to single events in the wind forcing, i.e. the arrival, presence and departure of low and high pressure system respectively. The model output is divided into time intervals of the same length. The direct comparison of both PDFs for the passing low pressure system
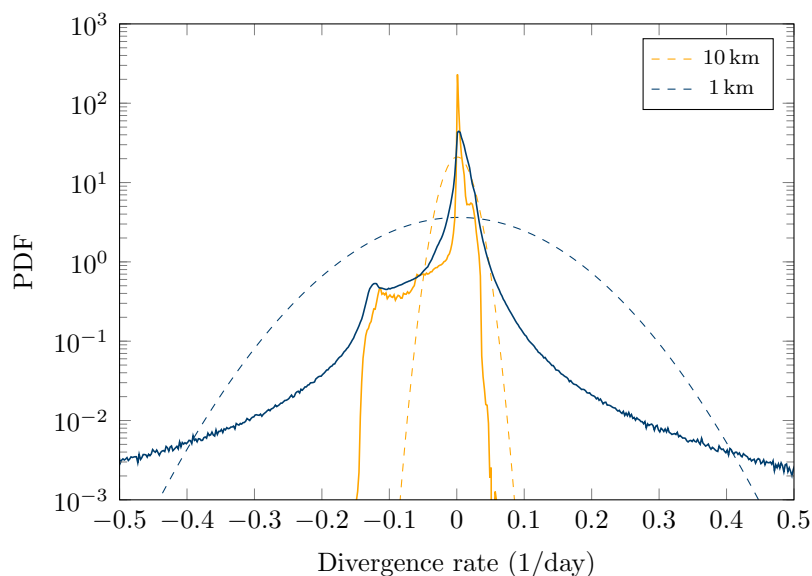
Figure 5.12: Comparison of PDFs of divergence rate ϵ_I for 10 km an 1 km resolution with Gaussian distributions, indicated by dotted lines. The Gaussian distributions are computed with the mean and standard deviations of the modeled divergence rate.

in Fig. 5.13 emphasizes a strong link between wind stress and sea ice deformation. The distributions resemble each other with the small differences in the magnitudes of strain rates, which are explained by a damping of the wind stress due to other terms in the momentum balance (2.1). Thus the peaks in the PDFs of the strain rates are linked directly to peaks in the PDFs of the wind stress. As the idealized wind forcing is a repeating sequence of the same pressure systems, the characteristics of the two wind fields related to low and high are amplified in the PDFs. However PDFs of observational wind fields are smoother due to larger variability in pressure systems recorded.

5.3.2 Localization of Strain Rates

A different approach quantifying the strong localization of high strain rates is to analyze the area fraction of the surface accommodating the largest 15 % and 50 % of the sea ice deformation. The results of this analysis are presented in Tab. 5.3. The area fractions decrease with refining resolution. The only exceptions are the smaller area fractions of the 10 km run compared to the 5 km run. The overall trend,
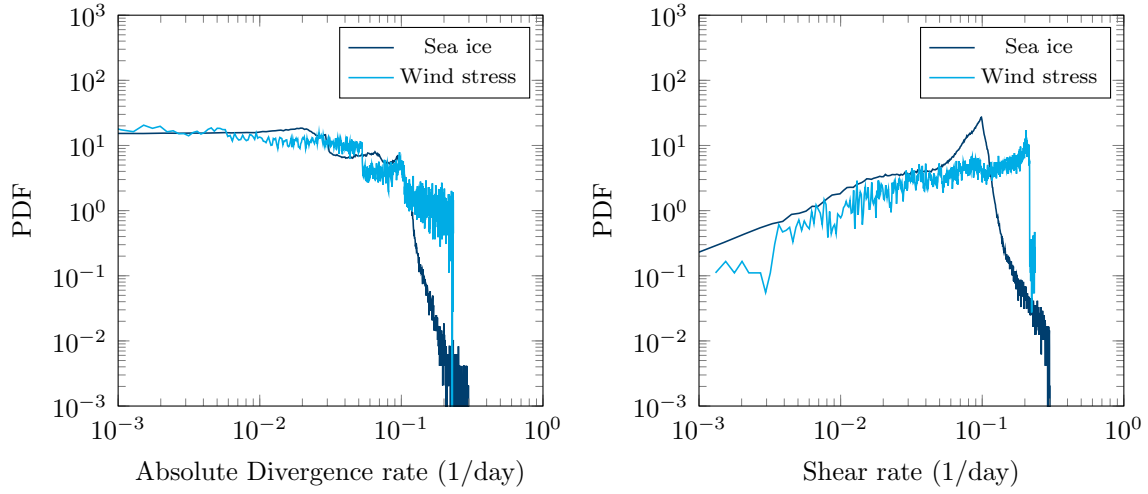
Figure 5.13: Comparison of PDFs of absolute divergence rate $|\epsilon_I|$ and shear rate ϵ_{II} for wind stress and model results. The presented time intervals corresponds to the presence of the low pressure system.

however, is also described for observational sea ice deformation data (Marsan et al., 2004; Girard et al., 2009; Stern and Lindsay, 2009). However, a direct comparison is only possible for the 10 km run as the length scales associated with observational values range from 10 to 100 km as noted in Section 3.2.2. At this scale the largest 15 % of the total deformation are located in 2.54 % of the surface, which is close to the observational values of 1.6 % (Marsan et al., 2004) and 2 % (Stern and Lindsay, 2009). Half of the shear is accommodated in 10.28 % of the surface compared to 6 % for RGPS data (Girard et al., 2009). Please note that at a model resolution of 10 km large scale LKFs are not fully developing, which might lead to a higher area fraction than for observations. Unfortunately, no observational data is described at the high resolution resolving the LKFs. The area fraction shown in Tab. 5.3, however, show clearly a tendency of a strong localization of strain rates with increasing grid resolution.

44

Table 5.3: Area fraction of the surface accommodating the largest 15 % and 50 % of the absolute divergence rate $\dot{\epsilon}_I$, shear rate $\dot{\epsilon}_{II}$ and total deformation $\dot{\epsilon}_{tot}$ in %.

Resolution		1 km	2 km	5 km	10 km
$\dot{\epsilon}_{\mathbf{I}}$	15 %	0.08	0.88	1.50	1.03
	50 %	2.38	5.66	9.02	6.50
$\dot{\epsilon}_{\mathbf{II}}$	15 %	0.26	1.29	3.24	2.64
	50 %	4.97	8.65	13.45	10.25
$\dot{\epsilon}_{\mathbf{tot}}$	15 %	0.26	1.51	3.40	2.54
	50 %	6.00	9.96	14.40	10.48

Chapter 6

Experiments with Reanalysis Wind Forcing

With the idealized wind forcing, the amplification of particular stress states induced by the regular recurrence of two pressure systems biases the PDFs of the strain rates. In contrast to the idealized wind forcing, pressure systems of various strength and spacial extent form the Arctic wind fields. The diversity in pathways of pressure systems and their interferences (interaction with each other) cause more randomized wind speeds as well as divergences and shear states. In the model this natural spread is expected to force a variety of stress state in the sea ice and thereby to smooth the PDFs of the strain rates.

Hence, simulations based on the previous model were carried that are out forced by reanalysis wind fields as described in Section 4.2.2. The analysis of the probability distributions and the multi-fractal characteristics of the modeling is presented in the following.

6.1   Statistical Properties of Modeled Sea Ice

The PDFs of divergence and shear rate in Fig. 6.1 and 6.2 are computed analogously to those in Section 5.3.1 for model runs driven with EMCWF high resolution wind forcing. The modeled sea ice is concentrated in the north east corner of the
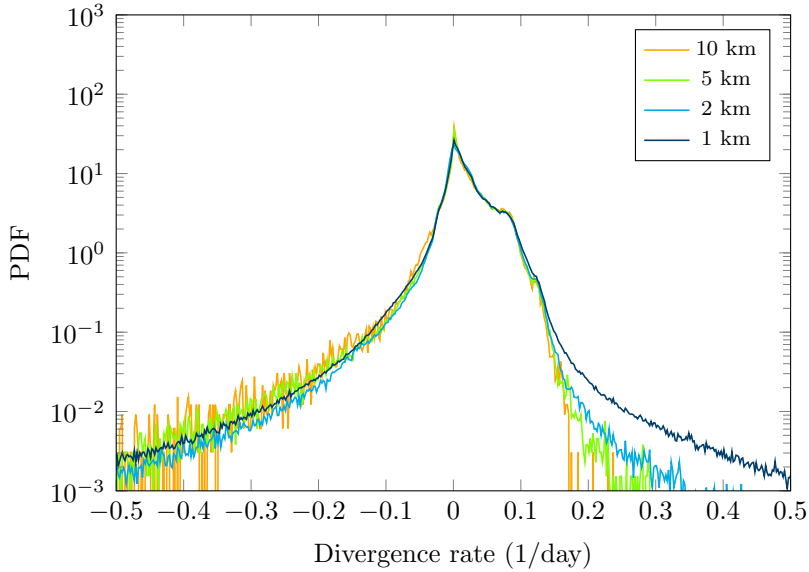
Figure 6.1: PDF of absolute divergence rate ϵ_I for different resolution in one month model results forced with ECMWF reanalysis data.

environment, because the mean flow of the wind forcing is filtered insufficiently (see Sec. 4.2.2). The converging states that entail the concentration of sea ice in the North East corner are clearly observable in Fig. 6.1 around $0.1\,\mathrm{day}^{-1}$. To attenuate the impact of the converging stress states on the PDFs, only one month of data is analyzed resulting, however, in noisier PDFs. In addition for determining the slope, the number of bins was reduced to 500.

The PDFs of all coarse resolutions are very similar except for the 1 km showing a higher amount of large convergence and shear states. In addition, the mean of divergence rate and shear given in Tab. 6.1 are of the same order of magnitude in all resolutions, which implies similar behavior in the simulation. However, the standard deviations double when increasing the resolution from 2 km to 1 km. The slope of the power law tails of the PDFs decreases drastically at this resolution.

The PDFs in Fig. 6.2 follow power law distributions with different slopes. For resolutions of 2 km, 5 km, and 10 km, the PDFs are on the border between Gaussian and Lévy attraction due to the power law exponent of ~ 3 for an absolute divergence rate. The PDFs for shear rate are clearly in Gaussian attraction with slopes of ~ 3.7. This observation is consistent with the analysis of Girard et al. (2009) using a coarse
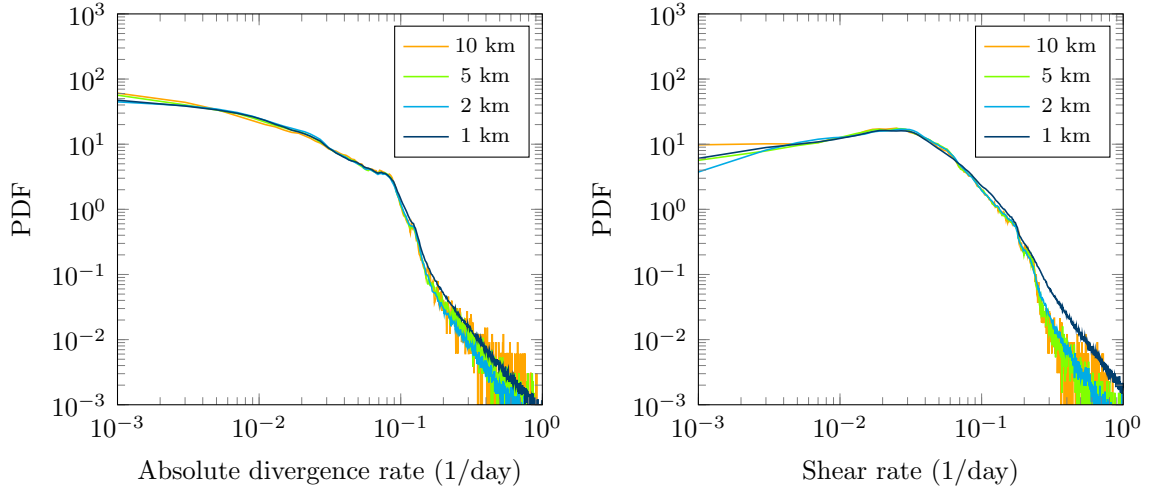
48

Figure 6.2: PDFs of absolute divergence rate $|\epsilon_I|$ and shear rate ϵ_{II} for different resolutions for one month (model results forced by JRA-25 reanalysis data).

Table 6.1: Mean and standard deviation (std) of divergence, shear rate, and ice speed for long term model runs forced with reanalysis wind forcing. The slope of the power law tails are determined from PDFs approximated by normalized histograms with 500 bins to reduce the noise.

Resolution		1 km	2 km	5 km	10 km
$\dot{\epsilon}_{\mathbf{I}}$	mean (day^{-1})	0.017	0.018	0.017	0.016
	std (day^{-1})	0.103	0.050	0.044	0.044
	Slope η	2.61	2.97	3.00	(2.81)*
$\dot{\epsilon}_{\mathbf{II}}$	mean (day^{-1})	0.055	0.049	0.048	0.047
	std (day^{-1})	0.127	0.054	0.045	0.045
	Slope η	2.85	3.71	3.76	(2.82)*
Ice speed	mean (m/s)	$7.98 \cdot 10^{-7}$	$7.05 \cdot 10^{-7}$	$6.92 \cdot 10^{-7}$	$6.86 \cdot 10^{-7}$
	std (m/s)	$1.85 \cdot 10^{-6}$	$7.69 \cdot 10^{-7}$	$6.21 \cdot 10^{-7}$	$6.21 \cdot 10^{-7}$
Number of observations		$1.64 \cdot 10^{7}$	$4.10 \cdot 10^{6}$	$6.55 \cdot 10^{5}$	$1.64 \cdot 10^{5}$

* The slope is determined for an interval including empty bins, which are neglected. This leads to increased and thus not comparable values.

model resolution of 12 km.

With RGPS derived power law exponents of 2.4 for absolute divergence and 2.5 for shear, Girard et al. (2009) concluded that sea ice models with VP rheology cannot be used to simulate sea ice deformation beyond the Gaussian attraction. Now this hypothesis can be challenged by the results of the 1 km run as well as the results with idealized wind forcing (Sec. 5.3.1). The distributions of the 1 km run with slopes of 2.61 for absolute divergence rate and 2.85 for shear rate are characterized by Lévy Laws, i.e. modeled sea ice deformation is dominated by extreme events. Both exponents approach observational values and demonstrate an enhanced localization of strain rate events along the modeled LKFs.

6.2 Multi Fractal Characteristics

6.2.1 Spatial Scaling Laws

The spatial scaling analysis presented in this section is adapted from the Lagrangian approach developed by Marsan et al. (2004) to Eulerian gridded data. The RGPS data analyzed by Marsan et al. (2004) is provided as trajectories of 40.000 points. They are initially distributed on a regular 10×10 km grid, but the grid deforms every time step. In this study however, the velocity and deformation output of the model is given on a regular grid fixed in space and time.

For a scaling analysis, a deformation over a range of different spatial scales is required. At the smallest spatial scale, the results of the simulation provide already the deformation. To determine deformation at larger spatial scales, the velocities are coarse grained yielding velocities on a grid with resolutions of different spatial scale. The velocity gradients are computed at all spatial scales and from these the deformation rates are calculated. The mean deformations for each spatial scale and for four different model resolutions are given in Fig. 6.3.

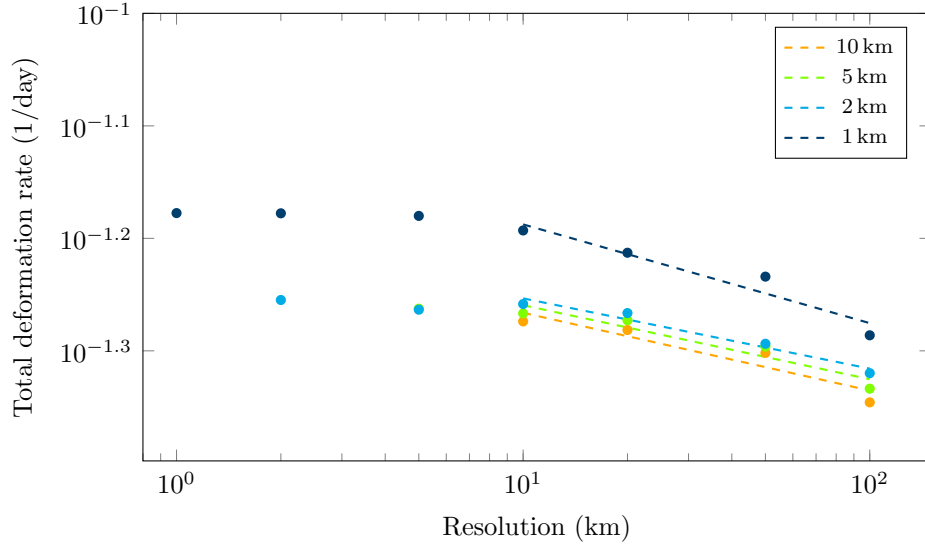The mean deformation decreases with increasing spatial scale due to the smooth-

Figure 6.3: Mean deformations for different spatial scales. The dotted line represents the least square fit to the power law (6.1). One month results of model runs at four resolutions forced with JRA-25 reanalysis wind data are used.

Table 6.2: Exponent of power-law scaling 3.4 (Slopes in Fig. 6.3) depending on resolutions for one month model output forced with JRA-25 reanalysis wind fields.

Resolution	1 km	2 km	5 km	10 km
Slope	0.088	0.063	0.066	0.069

ing of velocity fields. This decrease is approximated by a power law,

$$\langle \dot{\epsilon}\,(L) \rangle = C\,L^{-H}, \tag{6.1}$$

as described in Section 3.2.3. For all spatial scales, the mean deformation does not decrease linearly with the scale in the log-log-plot, as for small scales the mean deformation is almost constant whereas the mean deformation decreases beyond 10 km. This can be also seen in the resulting exponent (model resolution: 1 km) obtained in all spatial scales, which is rather small compared to observations. However, observations only cover spatial scales down to 10 km. Hence, only scales equal or larger than 10 km are considered for determining the spatial scaling coefficient, yielding to $H = 0.088$ (model resolution: 1 km).

In Table 6.2 the power law exponents for all resolutions are listed. For model resolutions between 2 km and 10 km the exponent varies only sightly, while there is a considerable increase when going to 1 km resolution. Scaling exponents for RGPS sea ice deformation data scatter around $H \sim 0.2$ (Marsan et al., 2004; Girard et al., 2009; Stern and Lindsay, 2009), which is twice the value of the 1 km resolution case. However Bouillon and Rampal (2015a) show that the scaling exponents could have been overestimated for total deformation by about 60 % due to insufficient filtering of the boundary definition error. In RGPS the deformation rates are estimated by a line integral, which requires precise information of the cell boundaries. The cells are defined by the four corner points leading to spurious area changes for cells that contain a pure shearing lead (Lindsay and Stern, 2003). The error in deformation rates induced by spurious area changes is called *boundary definition error*. This error is reduced by including more boundary points (Lindsay and Stern, 2003). The scaling exponent is about $H \sim 0.125$ when considering this overestimation (Bouillon and Rampal, 2015a). However, this value is still larger than the slope in the 1 km resolution simulation.

This gives rise to the question, why this and also other scaling exponents obtained for VP sea ice models (Girard et al., 2009, 2011) are too small. Girard et al. (2009) showed that the mean total deformation rate varies slightly for scales between 10 and 200 km. For larger scales, the mean deformation rate decreases similar to satellite
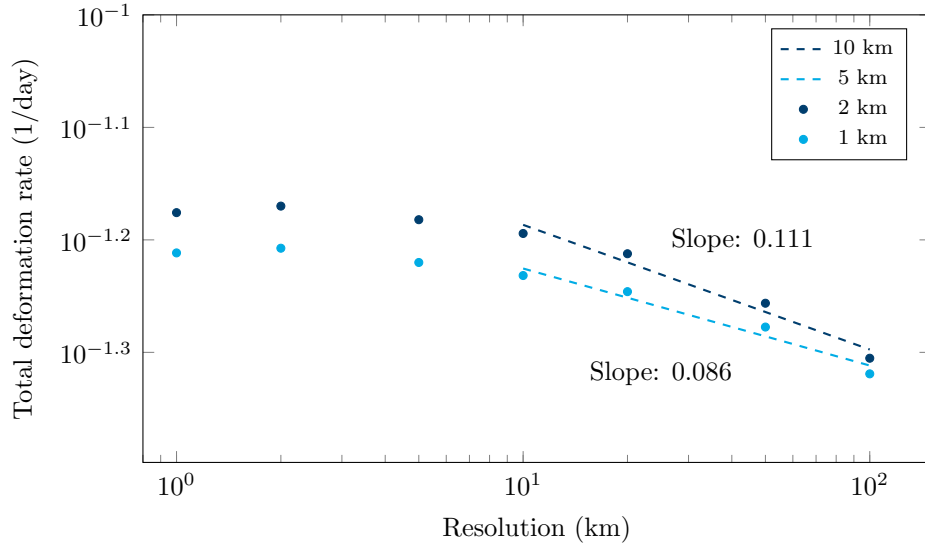
Figure 6.4: Spatial scaling of total deformation for two different wind forcing resolutions. For this analysis, 9 days of data of a model run with 1 km resolution and EMCWF forcing with 15 km and 125 km resolution is used.

observations. Recalling the wind forcing dependence of strain rate events (cf. Sec. 5.3.1), this threshold scale coincides with the resolution of the wind forcing ~ 125 km used by Girard et al. (2009). This suggests that high resolution wind forcing is maybe required to produce small scale deformation events in VP sea ice models.

The high resolution ECMWF forecast in 15 km resolution is used to study the effect of high resolution wind forcing on scaling properties of the modeled sea ice. The 1 km resolution model is forced with the high resolution wind data together with the same wind data coarsened by a 125 km running mean. Fig. 6.4 shows the spatial scaling analysis for both runs. The 15 km resolution wind forcing induces more small scale strain events between 10 and 100 km resulting in an increased slope of 0.111 compared to 0.086 for the reference wind resolution of 125 km. However for scales smaller than the wind resolution, no additional strain-rate events are generated as both curves are parallel in this regions. This supports the hypothesis that wind forcing is the main contributer to deformation events at small scales.

The spatial scaling exponent obtained with high resolution wind forcing is in better agreement with the observational values of $H \sim 0.125$ Bouillon and Rampal (2015a). It matches also the scaling coefficients produced by elasto brittle (EB) sea

53

ice models of $H = 0.1$ (Girard et al., 2011). EB sea ice models were developed to improve the deformation statistics over conventional VP models (Girard et al., 2011; Bouillon and Rampal, 2015b). However, the latest implementations of the EB rheology exhibit smaller scaling coefficients: $H = 0.04$ for shear rate and $H = 0.15$ for divergence rate (Bouillon and Rampal, 2015b).

Finally, the moments of the deformation rate are computed to further illustrate how the distributions of strain rates vary with the scale. The moments of the total deformation rate follow again a power law,

$$|\epsilon_{tot}^q|_L \sim L^{-\beta(q)}, \tag{6.2}$$

where q denotes the order of the moment and is chosen from the interval $q = 0.5, \ldots, 3$. Fig. 6.5(a) shows the calculated moments of total deformation along with the fitted power laws. The exponents of the power law $\beta(q)$ are referred to as the *structure function* (Bouillon and Rampal, 2015a). They are given in Fig. 6.5(b) as a function of the moment order q. The structure function $\beta(q)$ is quadratic $\beta(q) = aq^2 + bq$, where a is determined by a least square fit to 0.06. Marsan et al. (2004) obtained a quadratic shape of the structure function as well, although the estimated coefficient $a = 0.13$ is higher which indicates a higher degree of multi-fractality than found in our model simulation.

6.2.2 Temporal Scaling Laws and Time Space Coupling

Temporal scaling was detected in buoy observations tracking the ice motion (Rampal et al., 2008; Hutchings et al., 2011). The dispersion rate (Rampal et al., 2008) or the total deformation rate (Hutchings et al., 2011) is calculated for different temporal scales by varying the sampling rate of the trajectory positions. Hence the mean velocity for one temporal scale is determined by the ratio of the distance between two buoy positions $\mathbf{x}(t + T)$ and $\mathbf{x}(t)$ and the temporal scale T. In contrast to this, the model output is arranged on a regular grid providing velocity data for each time step and grid point. The velocity data is averaged over one temporal scale for one grid point to imitate the sampling rate. In theory both approaches yield the
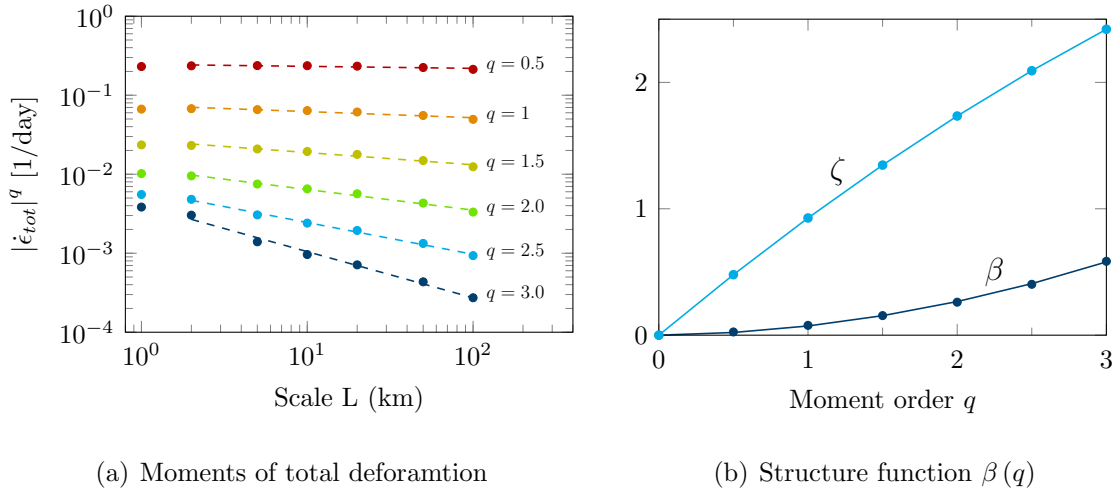
(a) Moments of total deforamtion (b) Structure function $\beta(q)$

Figure 6.5: Multi-fractal analysis: (a) moments of total deformation rate $|\dot{\epsilon}_{tot}|^q$ dependent on spatial scale L for $q = 0.5, \ldots, 3$ and (b) structure functions $\beta(q)$ and $\zeta(q) = q - \beta(q)$ as a function of the moment order q with least square fit to quadratic polynomial.

same results. However, note that the model output and the buoy trajectories are fundamentally different in their spatial coverage, spatial resolution and distribution of data points.

Nevertheless, the model results are examined for temporal scaling. To this end, the velocity data is averaged over several temporal scales, from which the deformation rates are computed. For each temporal scale, the mean total deformation is calculated and shown as a function of temporal scale in Fig. 6.6. This analysis is repeated for velocity data at different spatial scales to study space time coupling.

The mean deformation as a function of temporal scale separates in two different regimes as shown in Fig. 6.6. For temporal scales larger than 10 days, the mean deformation rate is decreasing with increasing scales as observed by Hutchings et al. (2011). For temporal scales between 3 hours and 10 days, the behavior strongly depends on the spatial scale in question. On large spatial scale ($50\,\text{km}$ and $100\,\text{km}$), the mean deformation decreases as well, but less strongly. In contrast, the mean deformation rate is increasing with increasing temporal scale on small spatial scale ($5\,\text{km}$ and $20\,\text{km}$) suggesting that the ice keeps some memory of deformation events over this period. The corresponding power law slopes are given in Tab. 6.3.
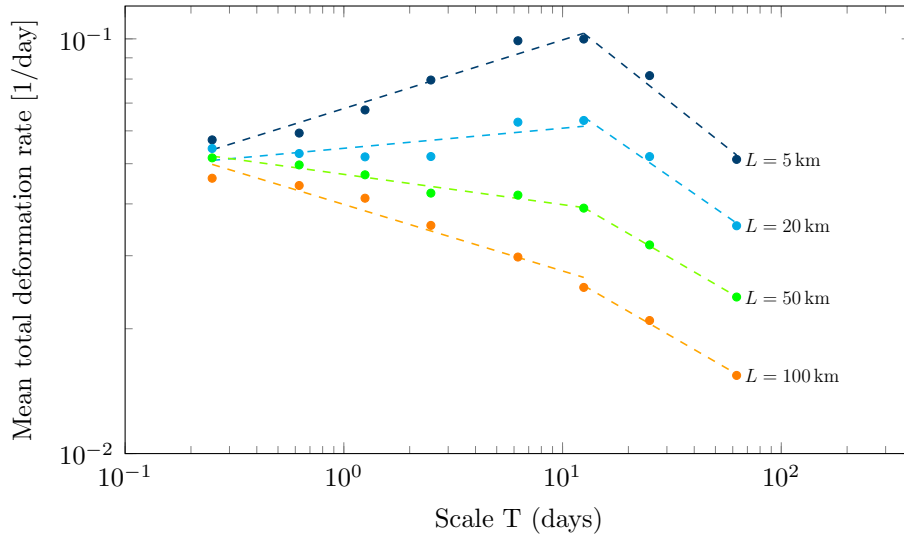
Figure 6.6: Temporal scaling of the mean total deformation for time scales between 3 hours and 62 days of an one year model run at 5 km resolution forced with JRA-25 reanalysis wind forcing. The analysis was performed at four different spatial scales 5 km, 20 km, 50 km and 100 km demonstrating a space time coupling. Least square fits to power laws are indicated by dashed lines for the two different regimes separated at a temporal scale of ~ 10 days. Sea ice concentrations of $A < 0.2$ are filtered in the data.

Table 6.3: Exponent of power-law scaling 3.7 (Slopes in Fig. 6.6) for different spatial scales. One year model run at 5 km forced with JRA-25 reanalysis wind fields is used for the analysis.

Spatial scale		5 km	20 km	50 km	100 km
Slope	$T < 10\,\text{days}$	-0.17	-0.05	0.07	0.16
	$T > 10\,\text{days}$	0.42	0.37	0.31	0.31

56

Hutchings et al. (2011) observed a decreasing mean deformation with increasing temporal scales with power law exponents close to one. Rampal et al. (2008) showed a decrease in the mean dispersion rate with increasing temporal scales as well. Both can only be observed for temporal scales larger than 10 days, although the scaling exponents only agree for the large spatial scales of $50\,\mathrm{km}$ and $100\,\mathrm{km}$ with summer observations of Rampal et al. (2008). They never reach the observed value of ~ 1 by Hutchings et al. (2011). The low scaling exponents characterize sea ice deformation as a mixture of viscous flow and single crack events dominated by viscous flow at large scale. The space time coupling described by Rampal et al. (2008) is apparent also for large temporal scales. However, it is less pronounced indicating less intermittent deformation processes in the VP model compared to observations.

Increased mean deformation with increasing temporal scale at small spatial scales is not described in the buoy studies (Rampal et al., 2008; Hutchings et al., 2011). Deformation events seem to accumulate in the averages of time scales up to 10 days, resulting in an increased mean. Exceeding the limit of 10 days, the smoothing effect in the gradient becomes dominant, and a decrease of the mean sets in. However, this phenomena is only observed in dense ice as the reference run without filtering low ice concentration shows in Fig. 6.7. Including all grid points in the analysis leads to curves resembling each other in slopes and deformation rates as observed by Hutchings and Hibler (2008), although the scaling exponents $\alpha = 0.3$ are smaller than those for buoy observations. Analysis filtered for higher ice concentration shows an enhanced "memory effect" (not shown here), and gives rise to the hypothesis that the results of Hutchings and Hibler (2008) are dominated by free drift ice floes and areas of open ocean. In this case the low scaling exponents could be explained with the model set up where ocean is at rest. The ocean at rest leads to artificial damping of sea ice motion. Hence, one can speculate that permitting ocean motion would accelerate the sea ice with low concentrations and result in higher velocity gradients and therefore strain rates.
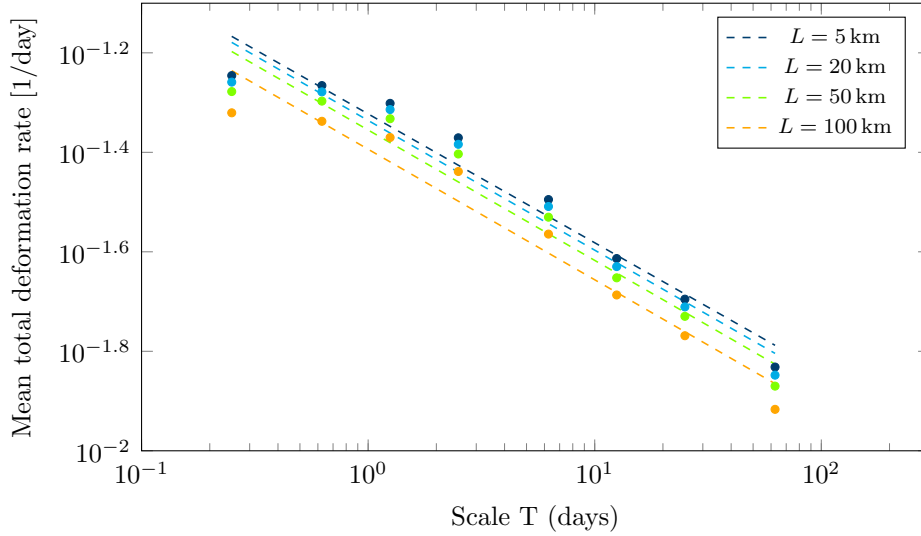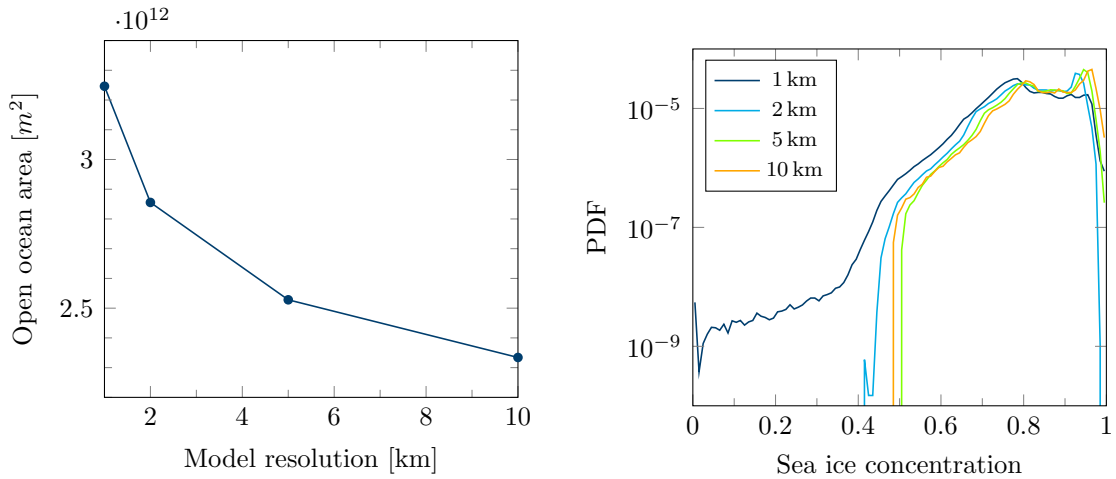
Figure 6.7: Temporal scaling of mean total deformation rate in the same data used in Fig. 6.6 but without filtering cells of low ice concentrations. The analysis is performed for different spatial scales. The dashed lines denote fitted power laws.

6.3 Open Ocean Area

The main motivation for a proper representation of LKFs in climate models is their strong impact on the interaction between ocean and atmosphere in the Arctic climate system. Major parts of the heat transport is located in leads and thus modeling these areas of open ocean is of particular interest.

The sea ice concentration is integrated over the environment to compute the area of open ocean in the ice pack. For this, the model runs in four different resolutions, forced with JRA-25 reanalysis wind data and lasting one month. The open ocean area is shown as a function of resolution in Fig. 6.8. The coastlines are removed for this analysis (outer 100 km) to account only for effects caused by LKFs in the dense ice pack instead of the motion of the entire ice cover.

The area of open ocean increases with increasing resolution in Fig.6.8(a) as the higher density of LKFs suggests. Pushing the model resolution to 1 km leads to additional 50 % of open ocean area compared to model results with 10 km resolution. The PDF of sea ice concentration (Fig. 6.8(b)) illustrates that the higher resolution model produces leads with very low sea ice concentration. For low resolution runs, the limit of low sea ice concentration is larger with 0.4.

(a) Changes in open ocean area depending on model resolution

(b) PDF of sea ice concentration (number of bins: 100)

Figure 6.8: Effect of modeled LKFs on the open ocean area and the distribution of sea ice concentration. One month of model output forced with JRA-25 reanalysis data is used for this analysis. The outer 100 km of the environment are ignored to study the effect of LKFs in the closed sea ice cover.

Hence, the increased amount of open ocean areas implies a larger heat transport in climate models with a high resolution sea ice component. Besides increased lead area, the shape of leads and the accurate determination of sea ice concentrations is a crucial factor to reproduce the atmosphere-ocean interaction properly (Lüpkes et al., 2008). Therefore, the increased open ocean area and the detailed PDF of sea ice concentration implies that heat transport changes for a high resolution sea ice model.

Chapter 7

Predictability

Two different types of model set-ups are used to test the predictability of the modeled LKFs. Firstly, the wind forcing is perturbed while leaving the initial conditions unchanged, and secondly, perturbed initial conditions are combined with the same idealized wind forcing. The experiments are designed to study the effect of uncertainties in the input data on the modeled LKFs assuming a perfect model. The 1 km resolution model is used for the predictability experiments.

7.1 Perturbed Wind Forcing

In current weather prediction models the surface wind fields of single ensemble members diverge within a few days. Since the wind stress strongly influences the LKF formation as shown in Section 5.3.1, diverging wind fields will change the position of LKFs. In this experiment, the sensitivity of LKF positions to uncertainties in the wind forcing is examined.

7.1.1 Experimental Set-Up

Wind fields of single ensemble members could be chosen as forcing to study the effect of the growing uncertainty in wind data. Due to data limitations not single ensemble members are used, but diverging "realistic" wind fields are constructed from the ECMWF high resolution forecast. For this purpose, the wind fields are
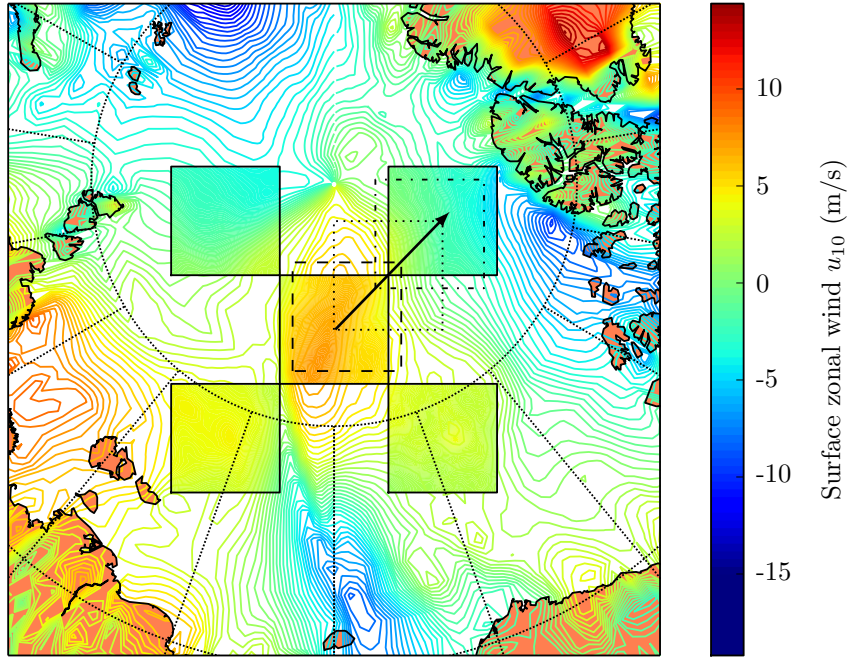
Figure 7.1: Wind field set-up used for predictability experiments. Final regions of interpolation are marked as filled contour plots inside the five squares. The central square is the reference run, where all ensemble members start. With progressing time, the interpolation area moves towards the final positions denoted by the squares at the corner. The movement in time is denoted for one box exemplary by dashed line for day 2, dotted line for day 4 and dash dotted line for day 6. The ECMWF high resolution wind field is used for interpolation.

interpolated in a 500 by 500 km box. The location of the interpolation box moves from a reference region to a final location over time to achieve diverging wind fields compared to the reference run. The location and motion of the interpolation areas is illustrated in Fig. 7.1. The transition lasts 8 days and follows a hyperbolic tangent to imitate appropriate divergence of the ensemble members. The correlation of each area with the reference area is given in Fig. 7.2. The decaying correlation with increasing time compares with the predictive skill of current weather prediction systems (Bauer et al., 2015), although the decay is slightly too fast.

7.1.2 Results

The five different wind fields, introduced in Section 7.1.1, force individual model runs using same initial conditions, from which one is considered the reference run.
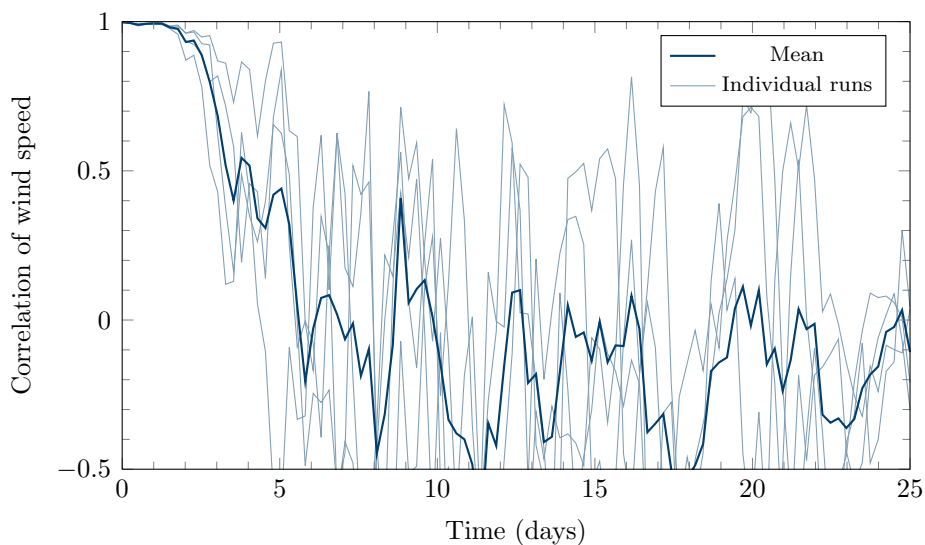
Figure 7.2: Correlation of four shifted wind fields with the reference fields in the center. The correlations of each area are presented as thin lines, the mean correlation is given as a thick line. After five days, the wind fields are decorrelated with a mean of -0.144.

A pick-up file of deformed sea ice is used, and the experiment lasts 25 days. The norm of the gradient of the sea ice concentration is computed to filter LKFs, because the gradient is large at the boundaries of a LKF. For each time step, gradient fields of all four runs are computed and the point-wise correlation between the calculated fields and the gradient field of the reference run is computed. The time series of these correlations are given in Fig. 7.3.

The correlation of LKF positions decreases as the divergence of the wind fields sets in (cf. Fig. 7.3). After five days the correlation drops below 0.5, however the wind forcing reaches this value already two days earlier. Beyond this point the LKF positions are mainly uncorrelated with a mean correlation of 0.13. Only taking into account regions of higher correlation, the divergence of LKF positions is delayed compared to the diverging wind fields by some hours. For a correlation of 0.8 the difference is 17 hours. This shows that the model can predict LKF positions to some extent, although a forecast skill is strongly limited by the quality of the wind field.

However, the point-wise correlation results only in large values if all LKFs are reproduced in same grid cells for both runs, i.e. with an accuracy of 1 km. Running means with intervals of 5 km and 20 km, respectively, are applied to test the
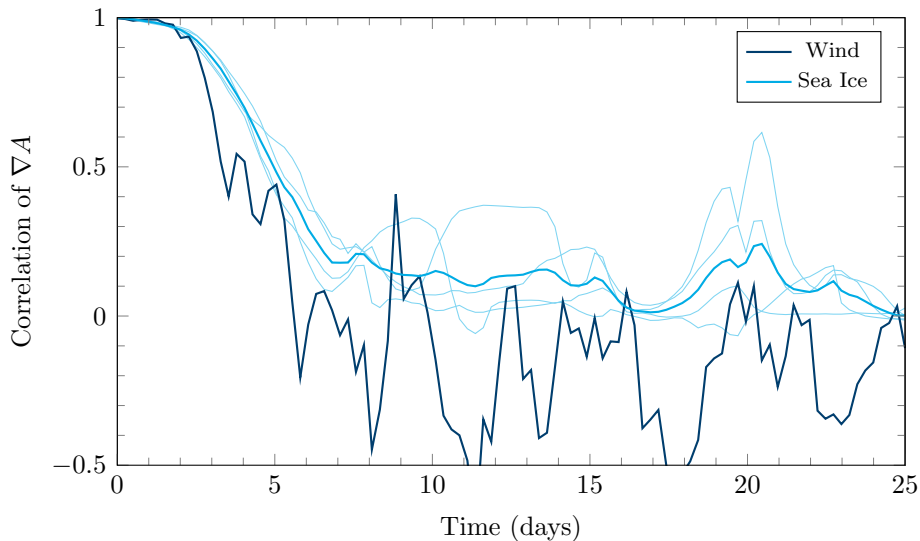
Figure 7.3: Mean correlation of four model runs with perturbed wind forcing to the reference run is shown in pale blue. The results of the individual runs are presented as thin lines. The correlation of the wind fields is given in dark blue. After five days the wind fields are decorrelated with a mean of -0.144.

predictability at "coarser accuracy". A comparison between all three accuracies is provided in Fig. 7.4.

The model shows higher predictive skill for coarser scales of LKF positions (Fig. 7.4). For a running mean of 20 km, the LKF positions still exhibit correlations of 0.9 after 5 days. The extension of predictability with coarsening the scales suggests local shifts of the LKFs (see Appendix C) for the period when the divergence of wind fields sets in. As all curves reach a quasi steady state after 10 days, the shifted LKFs have gradually cleared away, and the sea ice is covered by LKFs originating from completely diverged wind fields.

7.2   Perturbed Initial Conditions

The second set of experiments investigates the sensitivity to uncertainties in initial conditions. The experiments are started from a pick-up file generated by a model run with idealized wind forcing. The parameters of the pick-up file are perturbed. Therefore, the concentration and the thickness of the sea ice are increased and
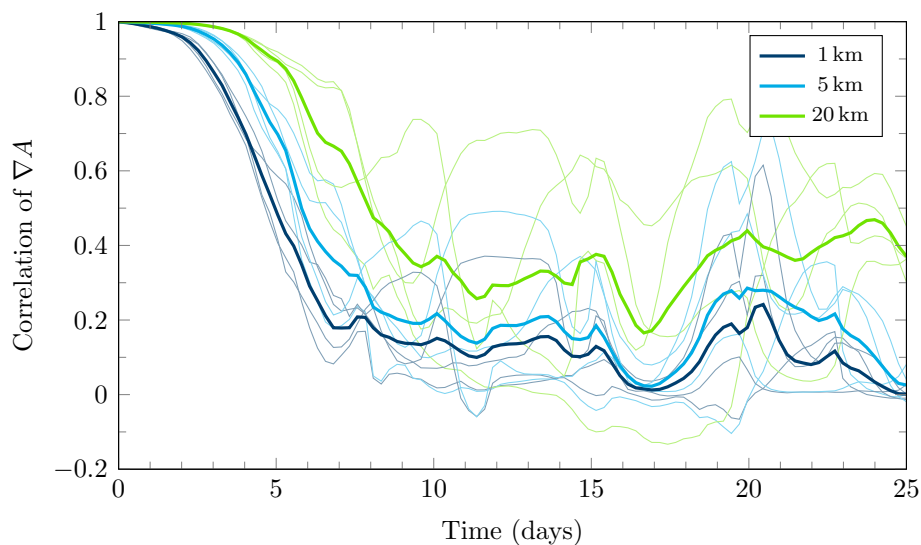
Figure 7.4: Mean correlations of LKF positions in four model runs smoothed by a running mean with different interval lengths, showing higher correlations for larger scales. The individual runs are given as thin lines.

reduced by 5 %. In a different configuration white noise of 5 % and 5 cm, amplitude, is added on its concentration and thickness. The increase of sea ice concentration is limited by 1. The last set of perturbed initial conditions is obtained by slightly deforming the grid of the pick-up file. The grid is both, stretched and shrunk, symmetrical as well as asymmetrical with regard to the wind forcing path, and also rotated in the center. The deformation is shown in Fig. 7.5.

The model runs are forced with the idealized wind forcing, because by its definition it introduces LKFs more efficiently in the ice cover compared to observational wind fields. As a tracer of LKF positions, the gradient of the sea ice concentration is filtered by a threshold. Gradients exceeding the threshold mark LKFs. Instead of directly correlate the arrays, the correlation of the masked arrays is used to damp the magnitude dependence in the computation of the correlation.

7.2.1 Sea Ice Concentration

The initial sea ice concentration is systematically and randomly perturbed by 1 % and 5 %. The sensitivity of the positions of modeled LKFs to these perturbations is given in Fig. 7.6. Variations in the sea ice concentration of the order of 5 %

65

(a) Symmetric stretch and shrink

(b) Asymmetric stretch and shrink
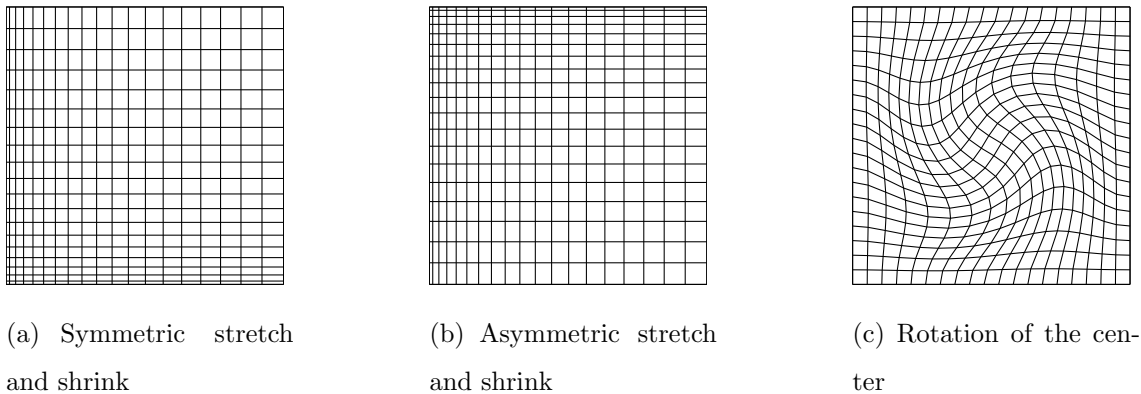
(c) Rotation of the center

Figure 7.5: Deformed grid, on which the initial conditions are interpolated. The degree of deformation is exaggerated here to better illustrate the grid deformation. The correlation between deformed and undeformed initial conditions in the experiment is 0.99.

have a strong impact on the formation and distribution of the modeled LKFs. The correlation drops drastically for all scales. Even at scales of 20 km the correlation falls below 0.5 within 5 days. The strong wind forcing leads to a homogenization of the sea ice concentration and accounts for the increase of correlation after 10 days. Better agreement between perturbed and reference run is achieved by limiting the uncertainty in the initial state to 1 %. In this case, a correlation of 0.9 is obtained after 4 days for 5 km accuracy and 6 days for 20 km scale. In addition, the correlation stabilizes around 0.8 for the 20 km scale, which is partly assigned to homogenization by the wind forcing.

Uncertainties of sea ice concentration observed from passive microwave radiometry range about 4 to 7 % (Kwok, 2002). Hence, a perturbation of 5 % as in the experiment seems to be reasonable. The sensitivity of the positions of modeled LKFs to the initial sea ice concentration is tremendous, although to some extend the choice of the tracer is responsible for that, as the correlation is determined from the masked gradient of the perturbed array.

7.2.2   Sea Ice Thickness

In this experiment, the initial sea ice thickness is enhanced and reduced by 5 % also white noise is added. The correlation of masked LKF position is presented in
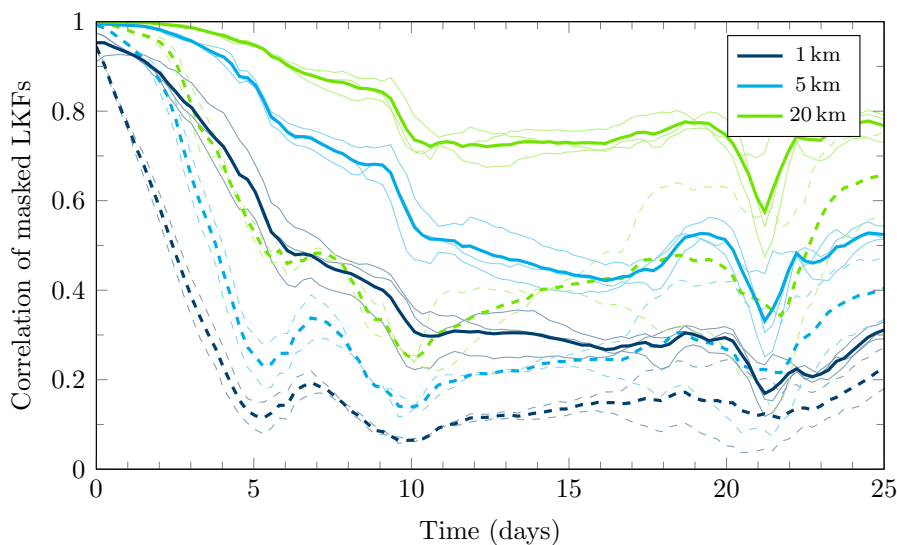
Figure 7.6: Mean correlation of LKF positions in three model runs with perturbed initial sea ice concentration. The solid lines represent perturbations of 1 % while the dashed lines represent perturbations of 5 %. A running mean is applied to test the accuracy of the modeled LKF positions. The individual runs are given as thin lines. There is no significant difference between systematic and randomly perturbed initial conditions.

Fig. 7.7.

For an accuracy of 5 km and 20 km, the LKF positions are highly correlated in the first five days showing correlation values higher than 0.95. After five days the correlation decreases slowly until a quasi-steady state is reached at day 15, in which the correlation is mainly affected by the wind forcing. The point-wise correlation decreases faster compared to the lower accuracies, and drops already below 0.85 at day 5. The difference between the systematic and randomly perturbed sea ice thickness is only significant for high accuracy within the first five days (see thin curves in Fig. 7.7). The model run perturbed with white noise predicts LKF positions slightly better than the systematic perturbed model runs (correlation of 0.9 at day 5). However, after the first five days the differences diminish.

In these experiments the perturbations applied to the initial sea ice thickness range between $\sim 1\,\mathrm{cm}$ (5 % of 20 cm mean thickness) for the systematic error and $\sim 5\,\mathrm{cm}$ for the white noise. Uncertainties in observed sea ice thickness are much larger. The errors in estimating the thickness of thick sea ice using satellite altimetry
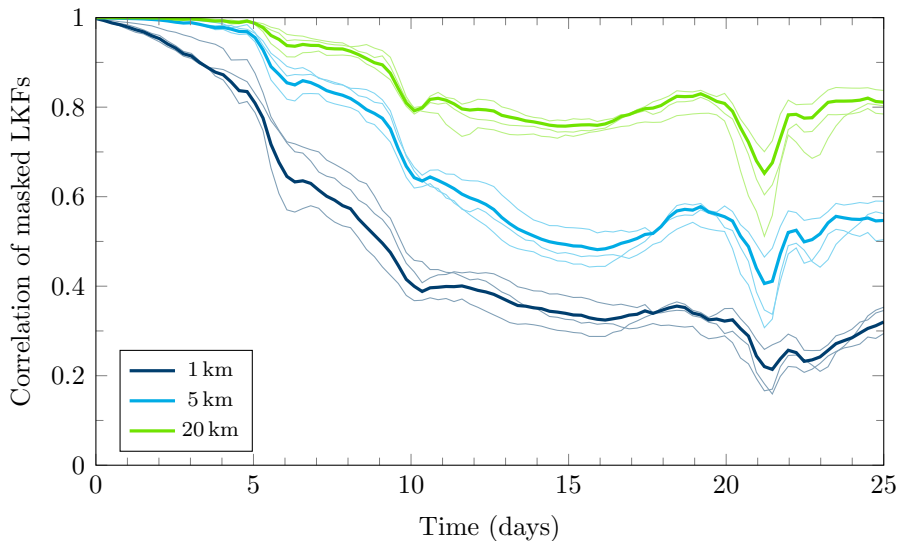
Figure 7.7: Mean correlation of LKF positions in three model runs with perturbed initial sea ice thickness smoothened by running mean with different interval lengths, showing higher correlation for less accuracy. The individual runs are given as thin lines. There is no significant difference between systematic and randomly perturbed initial conditions (thin lines).

are in the order of 0.7 m for ICESat (Kwok and Cunningham, 2008) and are mainly caused by a high uncertainty in estimating the snow depth. Using passive microwave remote sensing, the sea ice thickness up to half a meter is determined from brightness temperatures causing an uncertainty of 50 % (Kaleschke et al., 2012). The highest precision is achieved by electromagnetic (EM) ice thickness surveys with estimated errors of 0.1 m (Haas et al., 2010). However, the spatial and temporal coverage of this data is strictly limited. With these large uncertainties in observational data, a precise definition of the initial fields as in these experiments are not possible, and more rapid divergence of the deformation fields have to be expected for initial fields based on observational data.

7.2.3   Grid Deformation

The experiments with a deformed grid of the initial states are thought to imitate the position uncertainty in sea ice concentration and thickness products. The correlation of the position of LKFs between the perturbed runs and the reference run is shown in Fig. 7.8. The initial conditions on the deformed grid are interpolated to be used
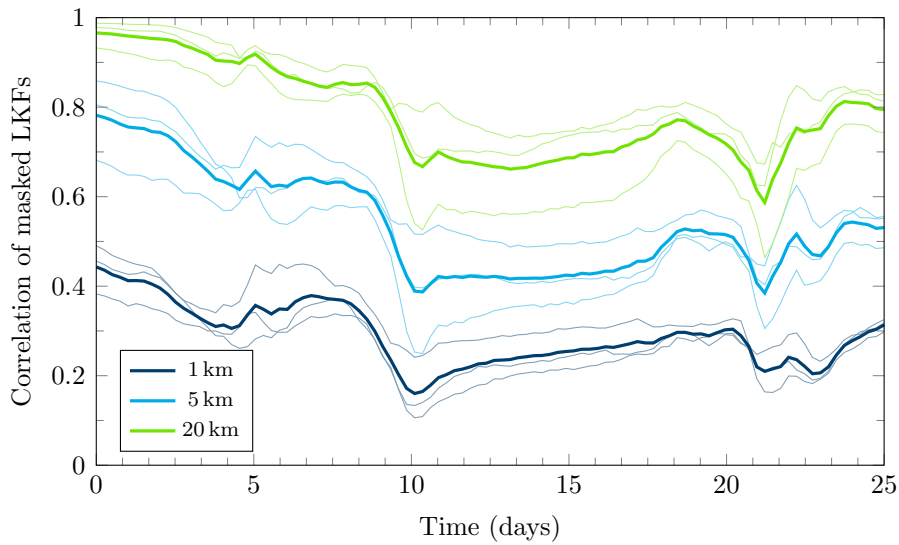
Figure 7.8: Mean correlation of LKF positions in three model runs with perturbed initial conditions by grid deformation. The thick lines represent different accuracy levels. The individual runs are given as thin lines.

in the model. However, this interpolation results in an artificial smoothing of the sea ice concentration, which causes strong deviations in marked LKFs as the gradient of the sea ice concentration is used for filtering. This results in low correlations as presented in Fig 7.8, showing that this way of creating ensemble members leads to meaningless results. Thus, the effect of position errors in the initial conditions has to be determined with a different approach. However, a stabilization effect of the correlation is observed after 10 days in this run as well.

Chapter 8

Conclusions

8.1 Model Resolution Dependence

The representation of LKFs in a sea ice model with viscous-plastic rheology raises strongly with resolution: at coarse resolutions of 10 km, the model results provide only a few LKFs, whereas for very high resolutions of 1 km an ample amount of LKFs spreads in the modeled sea ice cover. It confirms the observations of Overland and Ukita (2000), Maslowski and Lipscomb (2003), and Hutchings et al. (2005) stating that the VP rheology reproduces LKFs at high resolutions. However, the spatial resolutions used in those studies did not exceed 9 km. A detailed evaluation of model runs with resolutions up to 1 km is novel and reveals interesting insights in the behavior of the VP rheology at these scales.

Localization of Strain Rates

In strong correspondence to observations, LKFs mark regions of high strain rates in the model. The increasing amount of LKFs with refining resolutions leads to an intensifying localization of strain rates along these features. The localization manifests itself with higher probabilities of large strain rate events. The PDF of the deformation rates leave the Gaussian attraction satisfying Lévys law instead.

The 12 km resolution VP model of Girard et al. (2009) did not show these power law characteristics, leading Girard et al. (2009) to conclude that the VP rheology

is an inappropriate modeling framework for ice deformation. The results presented in Chapter 5 and 6 challenge these findings, as sea ice deformation rates possess power law characteristics for very high resolutions. At spatial resolutions of $1\,km$ the power law exponents coincide with satellite observations (Marsan et al., 2004; Girard et al., 2009). In contrast, for coarser resolutions of $10\,km$ the PDF of total deformation rate is in Gaussian attraction as Girard et al. (2009) showed. Therefore it is recommended to use spatial resolution not coarser than $2\,km$ to leave Gaussian attraction (Slope η in Table 5.2 must meet $\eta < 3$), if proper reproduction of sea ice deformation is desired.

Resolution Dependence of Parameter P^*

The resolution study revealed different dynamic behavior of the sea ice model with varying spatial resolutions. In high resolution runs an increased amount of viscous deformation is observed causing a delayed onset of plastic deformation. The ice strength is adapted to account for this effect and a complex resolution and ice strength dependence of the break up point is found. The results in Section 5.2 suggest a highly non-linear relation between the ice strength P^* and the spatial resolution in accordance to Overland and Pease (1988), and show that P^* is not a scale invariant parameter. Since P^* is often a tuning parameter in studies with fixed resolution, an optimal P^* is approximated to approach observations. However, if different resolutions are used in the study, a resolution dependent choice of P^* is necessary to keep comparable model results for different resolutions. Alternatively, P^* has to be tuned for each resolution used. The resolution dependence of P^* is of particular importance for sea ice models based on an unstructured mesh (Danilov et al., 2015) due to varying resolutions used in the model.

New Regime at Very High Resolutions?

The density and high abundance of LKFs in the very high resolution $1\,km$ run are remarkable, and distinguish this run from the lower resolution runs. In the statistical analysis in Chapter 6 the results for the $1\,km$ run differ strongly from coarser runs.

This gives rise to the question, whether a change in regime is taking place when refining resolutions from 2 km to 1 km. The study of resolution dependent dynamic behavior of the VP model show a gradual change (see Sec. 5.2) in contrast to the other observations. To finally answer this question, further analysis of model runs with intermediate resolution steps are needed. Nevertheless, the dynamic behavior seems to change exponentially with refining resolution at this very high resolutions.

8.2 Scaling Properties of Modeled LKFs

The modeled sea ice deformation is tested for spatial and temporal scaling laws. The obtained scaling characteristics are compared to satellite observations for spatial scaling (Marsan et al., 2004; Girard et al., 2009; Stern and Lindsay, 2009) and to buoy trajectories for temporal scaling (Rampal et al., 2008; Hutchings et al., 2011).

Wind Forcing Resolution

The main limitation of spatial scaling laws derived from VP sea ice models so far was the insufficient amount of small scale deformation (Girard et al., 2009). If the model resolution is refined, more small scale strain rate events are induced in the sea ice cover. However, as shown in Section 6.2.1 this increase is insufficient to reproduce observational scaling exponents. Still an enhancement of the wind forcing resolution leads to additional small scale deformation. Combining both effects results in scaling law exponents comparable to satellite observations. The derived scaling laws are of the same quality compared to the EB rheology (Girard et al., 2011; Bouillon and Rampal, 2015b), which was designed to reproduce accurate scaling characteristics. Hence, the VP rheology can be used to model LKFs, although the strong link between sea ice deformation and wind forcing demands high resolution wind forcing. The resolution of the wind forcing should coincide with the smallest scale, for which scaling laws match with observations.

Memory Time of LKFs

The temporal scaling analysis of dense ice shows increasing mean deformations for increasing temporal scales up to a scale of 10 km. This increase can be seen as an accumulation of different deformation events with a memory of ten days (c.f. Sec. 6.2.2). After this time span, the information of the deformation event is lost, and the more pronounced smoothing results in a decrease of mean deformation rates for larger time scales. The predictability studies, presented in Chapter 7, support this hypothesis as for all initial conditions studies the correlation has decreased to a quasi-steady state after ten days (Fig. 7.6, 7.7 and 7.8). The information of the LKFs in the initial state causes the correlation between two fields. With progressing deformation of the initial state the information of the initial LKFs is lost until after ten days no traces of similarity can be found.

This memory effect is so far not reported in observational data (and cannot be reported), since the temporal and spatial resolutions are too low to filter deformation rates of dense ice for temporal scaling. The RGPS data has an initial spatial resolution of 10 km, which is sufficient to filter dense ice. But the temporal resolution of three days limits the exploration of temporal scaling laws. Buoy data exhibit excellent temporal resolution, but the low spatial coverage prohibits further spatial filtering. Furthermore, additional information of sea ice concentration is needed to select only buoys in dense ice. Therefore, the temporal scaling of buoy data is dominated by free drifting ice as illustrated in Section 6.2.2. Finally, the acquisition rate of satellites needs to be raised to explore the memory of sea ice deformation in observational data.

8.3   Predictability

The predictability experiments carried out in the idealized environments reveal a strong sensitivity of the modeled LKFs to the accuracy of the wind forcing and the initial conditions. The divergence of LKF positions is strongly related to the diverging wind fields, although. The model shows predictive skill of roughly one day

depending on the scale. This strong wind forcing dependence is already observed in the PDF of sea ice deformation rates in Section 5.3.1. The second predictability experiments are initialized with perturbed sea ice concentration and sea ice thickness data. Perturbations of 5 % in sea ice concentration have a strong impact on the positions of modeled features. Restricting the position accuracy to 20 km enables a reasonable forecast over two days. Modeled LKFs are less sensitive to perturbations in the sea ice thickness of the same order. This makes determining of LKF positions over a time span of 8 days possible at an accuracy of 20 km. However, uncertainties in observational data exceed 5 % by far, and lead presumably to shorter predictive skill.

A potential forecasting system for LKFs has to face all named uncertainties simultaneously: With the high sensitivity of the modeled LKFs to single perturbations, the combination of all effects may even reduce the performance of the model in reproducing accurate positions of LKFs. Initializing the model with high-quality data assimilation output, LKF positions might be forecasted for 1 or 2 days, if high precision wind forcing is used.

Other metrics to evaluate predictability of sea ice deformation may show more promise, as the prediction of the exact position of LKFs is challenging. The density of modeled LKFs is less sensitive to shifted positions of LKFs than the point-wise correlation used in this study. Thus the predictive skill of the model to determine areas with high density of LKFs is expected to be higher than the results of this study. Probability maps of lead formation areas are useful tools to illustrate predicted sea ice deformation. In addition, regions of converging ice states could be forecasted for longer periods than the actual position. Both information of lead density and regions of converging ice are of interest and importance for shipping and economic activity.

Chapter 9

Outlook

In recent times of climate change the Arctic climate system faces a vast reduction of sea ice. Several positive feed-back mechanisms accelerate the melting: a decreasing albedo increases the absorption of shortwave radiation, which causes further melting (Curry et al., 1995). In addition, the thinning sea ice cover is more prone to fracturing by Arctic storms (Asplin et al., 2012) enhancing the sea ice-albedo feed-back cycle. Based on the decline of Arctic sea ice, the economic interest in polar regions substantially rises and Trans-Arctic shipping will intensify (Smith and Stephenson, 2013). Hence, further research is needed to better understand the role of LKFs in the Arctic climate and to forecast the presence of leads more reliable.

First the results obtained for the idealized environment in this study have to be confirmed in a run with realistic Arctic geometry. A scaling analysis of deformation could reveal further insight in seasonal variability and dependence on sea ice condition, like concentration and thickness, as outlined by Stern and Lindsay (2009). A set up including an active ocean model offers the opportunity to explore the effects of large scale forcing of ocean current and tides on LKFs.

To study the influence of LKFs on the Arctic climate, a high resolution sea ice model needs to be implemented in a coupled climate model. Despite the high importance of leads, the processes in the ocean-sea ice-atmosphere interaction are not fully understood. Although many subprocesses accommodated in leads are well described, e.g. convection in the atmosphere above leads (Lüpkes et al., 2008),

their interaction is not fully understood and has not been modeled so far in its entire complexity in a global framework. A coupled run could show how all involved processes influence each other and one could identify the interaction of different feedback mechanisms.

Coupling a very high resolution sea ice model to a climate model, long term climate projections can be performed to reveal the role of LKFs on global climate and answer the following questions:

- Do the changed sea ice dynamics drive a faster retreat of Arctic sea ice or lead to an ice free Arctic sooner?

- Do an enhanced heat flux in winter and increased absorption of shortwave radiation in summer intensify the polar amplification in an overall warming climate?

- What is the influence of changing conditions in polar regions on the global climate? Do the global circulation patterns change or is there mainly regional impact?

Appendix A

Impact of the Boundary on Modeled LKFs

This experiment examines the impact of the boundary shape on the orientation of the modeled LKFs. Boundary constraints initiate together with wind and ocean forcing the fracturing of sea ice. The aim of this experiment is to understand whether the shape of the boundary or the patterns of the wind forcing mainly influence the modeled LKFs. Besides the quadratical environment, a circular environment with an diameter of $500\,\mathrm{km}$ is implemented. Both environments are forced with the idealized wind forcing.

Time series of modeled sea ice concentration of both runs is presented in Fig. A.1. Although the shapes of the boundaries are fundamentally different, most LKFs observed in both runs show similar orientation. Especially after passage of the passage of the low pressure system, the leads in the sea ice coincide for both environments (seen in (b) and (f) as well as (l) and (p)). Although, there is agreement in all other time steps as well. The difference of the LKFs close to the boundaries shows the influence of the boundary. However, the good agreement in the ice pack underlines that the wind forcing mainly determines the modeled LKFs.
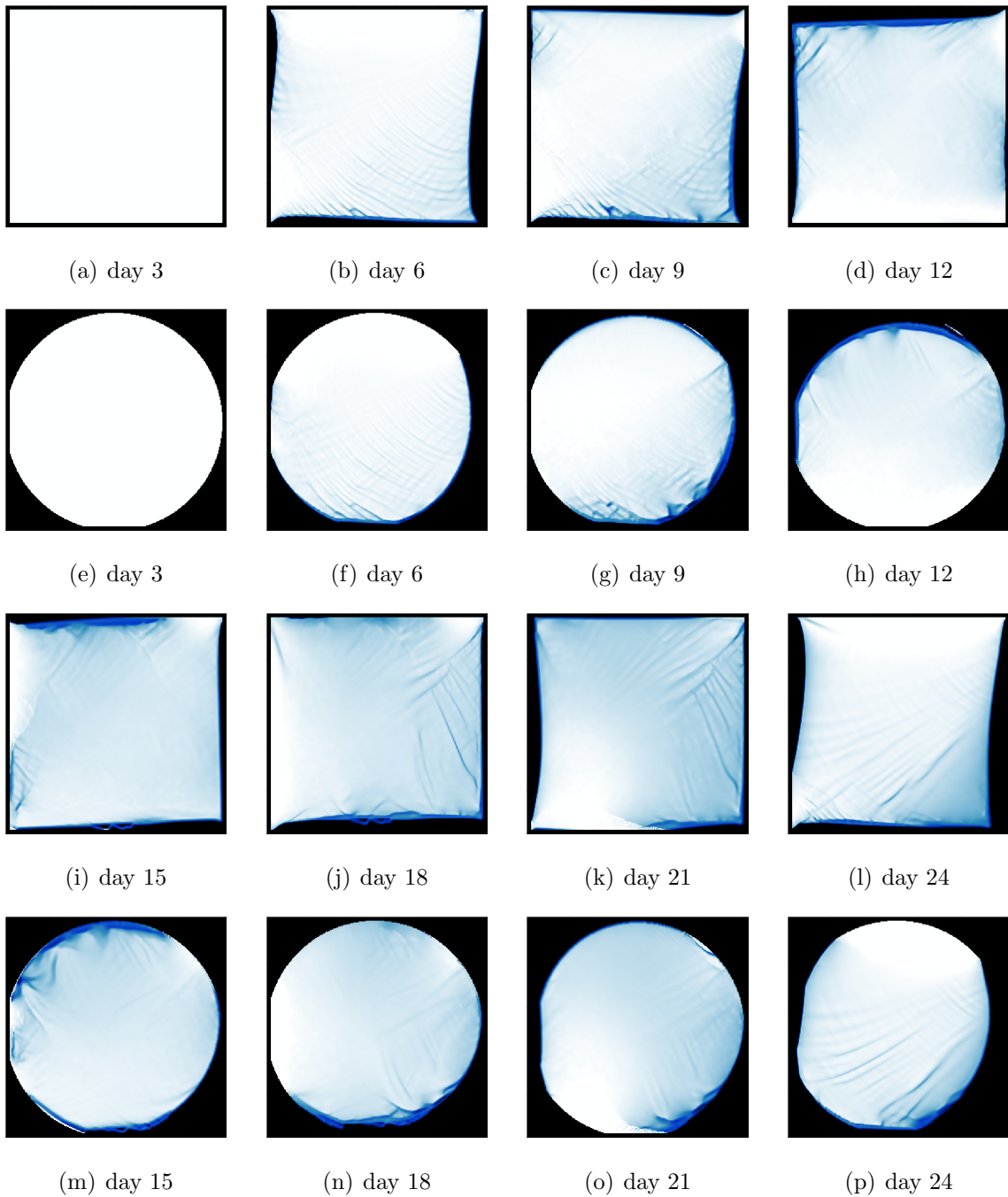
(a) day 3   (b) day 6   (c) day 9   (d) day 12

(e) day 3   (f) day 6   (g) day 9   (h) day 12

(i) day 15   (j) day 18   (k) day 21   (l) day 24

(m) day 15   (n) day 18   (o) day 21   (p) day 24

Figure A.1: Time series of modeled sea ice concentration A for quadratic environment and circular environment. The resolution of both runs is $2\,\mathrm{km}$. The same colorbar as in Fig. 5.1 is used.

Appendix B

Ice Strength Dependence for Idealized Forcing

In Chapter 5, a function (5.7) is derived to estimate the ice strength P^* for different resolutions in such way that the break-up point for both resolutions coincides. The relationship (5.7) was determined for a steady wind forcing representing the presence of a low pressure system.

Using the complete idealized wind forcing, however, the ice strength estimated with (5.7) improves the deviations in the break-up point for different resolutions only insufficiently. Thus, the same analysis presented in 5.2.2 is repeated using the complete idealized wind forcing.

The break-up point t_b is again a linear function of the ice strength P^* for a constant resolution Δx as presented in Fig. B.1,

$$t_b\left(P^*, \Delta x = const\right) = a\left(\Delta x\right) \cdot P^* + b\left(\Delta x\right). \tag{B.1}$$

The Ansatz functions (5.4) and (5.5) does not properly fit the observed break up point. Therefore, different Ansatz functions fulfilling the constraints (5.2) and (5.3) are introduced,

$$a\left(\Delta x\right) = \beta \Delta x^{\alpha}, \tag{B.2}$$

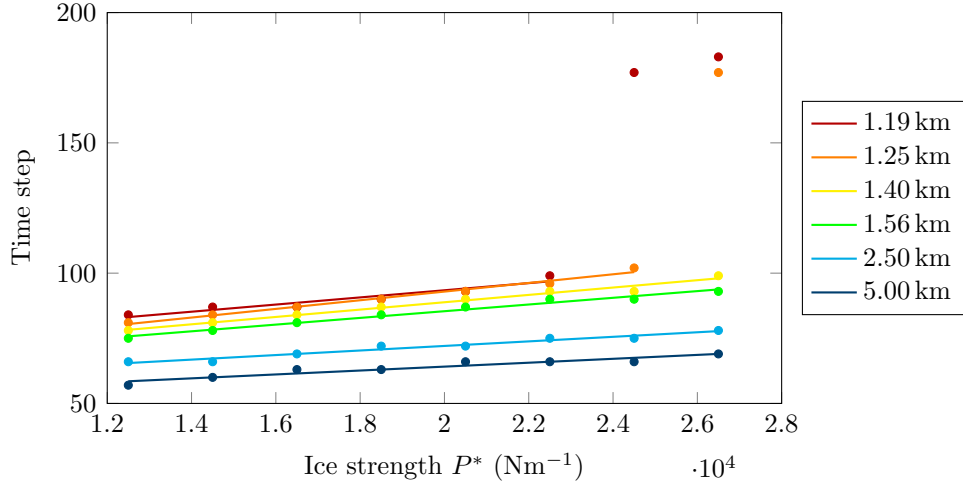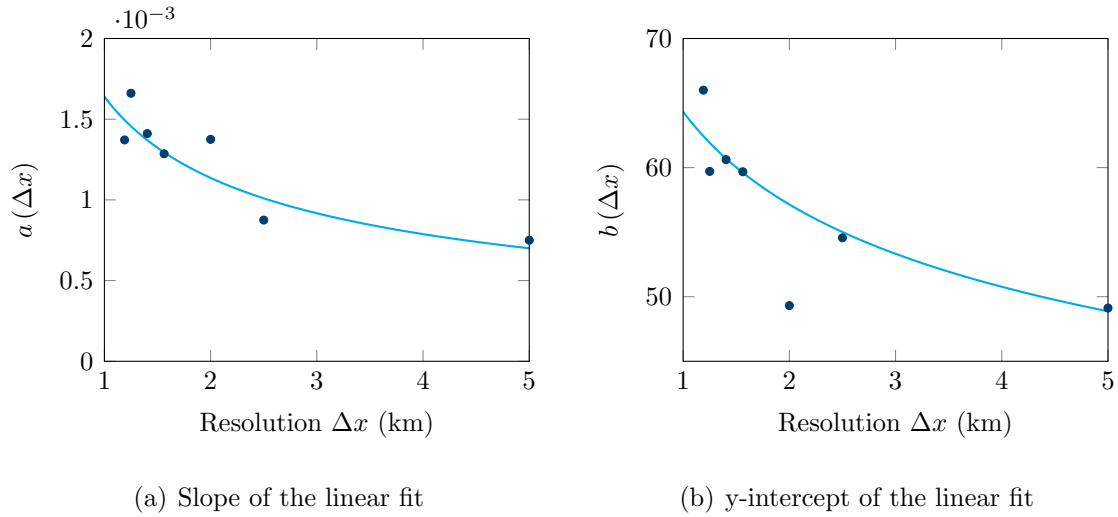$$b\left(\Delta x\right) = \delta \Delta x^{\gamma}. \tag{B.3}$$

Figure B.1: Break-up time as a function of the ice strength for different resolutions indicated by different colors. The break-up time steps are linearly increasing with the ice strength.

(a) Slope of the linear fit

(b) y-intercept of the linear fit

Figure B.2: Resolution dependence of the coefficients $a(\Delta x)$ and $b(\Delta x)$ of the linear relationship (B.1). The coefficients for the 1 km and 2 km run are outliers and therefore neglected in the least square fits presented in pale blue.

Table B.1: Coefficients determined with a least square fit of the coefficient functions to the model results of break up points.

α	β	γ	δ
-0.528	-1.201	-0.171	2.320

The unknown coefficients α, β, γ, and δ are determined by a least square fit to the model results[1]. The obtained results are given in Tab. B.1. Hence the final function of the break up time is,

$$t_b \left(P^*, \Delta x \right) = \beta \Delta x^\alpha \cdot P^* + \delta \Delta x^\gamma \tag{B.4}$$

The ice strength P_1^* for a resolution Δx_1 that lead to the same break-up point as P_2^* at the resolution Δx_2 is determined by,

$$P_1^* = \frac{\Delta x_2}{\Delta x_1} P_2 + \frac{\delta}{\beta \Delta x_1^\alpha} \left(\Delta x_2^\gamma - \Delta x_2^\gamma \right). \tag{B.5}$$

Fig. B.3 compares the observed break-up points with the fitted function (B.4). Except for the break-up points in the regime of the high pressure system (indicated with diamond shape in Fig. B.3), both coincide very well. The overall *root mean square error* (RMSE) is 2.631 time-steps. Regarding the low RMSE, the relationship B.5 is a suitable tool to estimate the ice strength that has to be used for different spatial resolution to obtain a comparable dynamic behavior. However, the difference between the two functions (5.7) and (B.5) shows that the estimated break-up point strongly depends on the wind forcing.

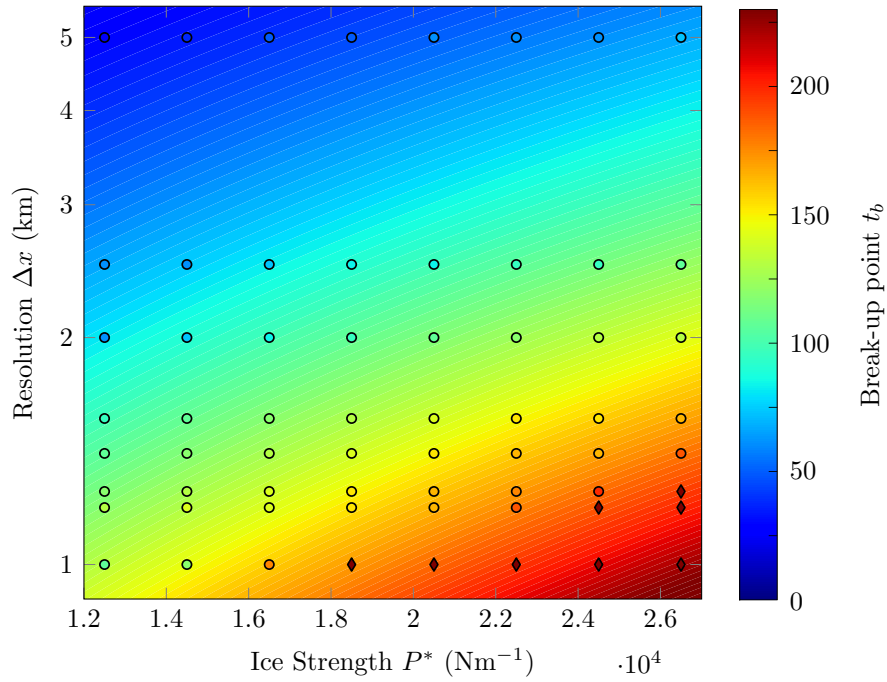[1]Resolutions 1 km and 2 km are neglected as an outlier in this estimate.

Figure B.3: Comparison of fitted break-up time as contour plot and observed break-up time in model results as points for the complete idealized wind forcing. Break-up points taking place during the passage of the low pressure system are marked by circles. Break-up point occurring during the passage of the high pressure system are diamond shaped and neglected in the fits (B.2) and (B.3). Configurations of resolution Δx and ice strength P^* resulting in the same break up point lay on the same contour line shown (equal color).

Appendix C

Shift of LKFs in Predictability Experiments

In Chapter 7, the shift of LKFs in different ensemble members is discussed. A running mean of different interval length is introduced to account for this effect. In Fig. C.1 the shift of LKFs in three ensemble members is presented in a RGB image. Each color channel shows the masked LKFs of a single ensemble member. In doing so, LKFs that appear in all three ensemble members are white. Leads in red, green and blue are only observed in one of the ensemble members, whereas leads in combination color are found in two ensemble members.

In the beginning, only white LKFs are observed (cf. Fig. C.1(a)) indicating the LKFs in all runs coincide. The amount of colored LKFs increases gradually as the divergence of the three model runs sets in. After five days, the majority of the LKFs is colored, which matches with the low correlation of LKFs position for this time in Fig. 7.6. The shift of the LKFs is seen by the many colored LKFs sharing the same orientation.

(a) day 0   (b) day 1   (c) day 2

(d) day 3   (e) day 4   (f) day 5
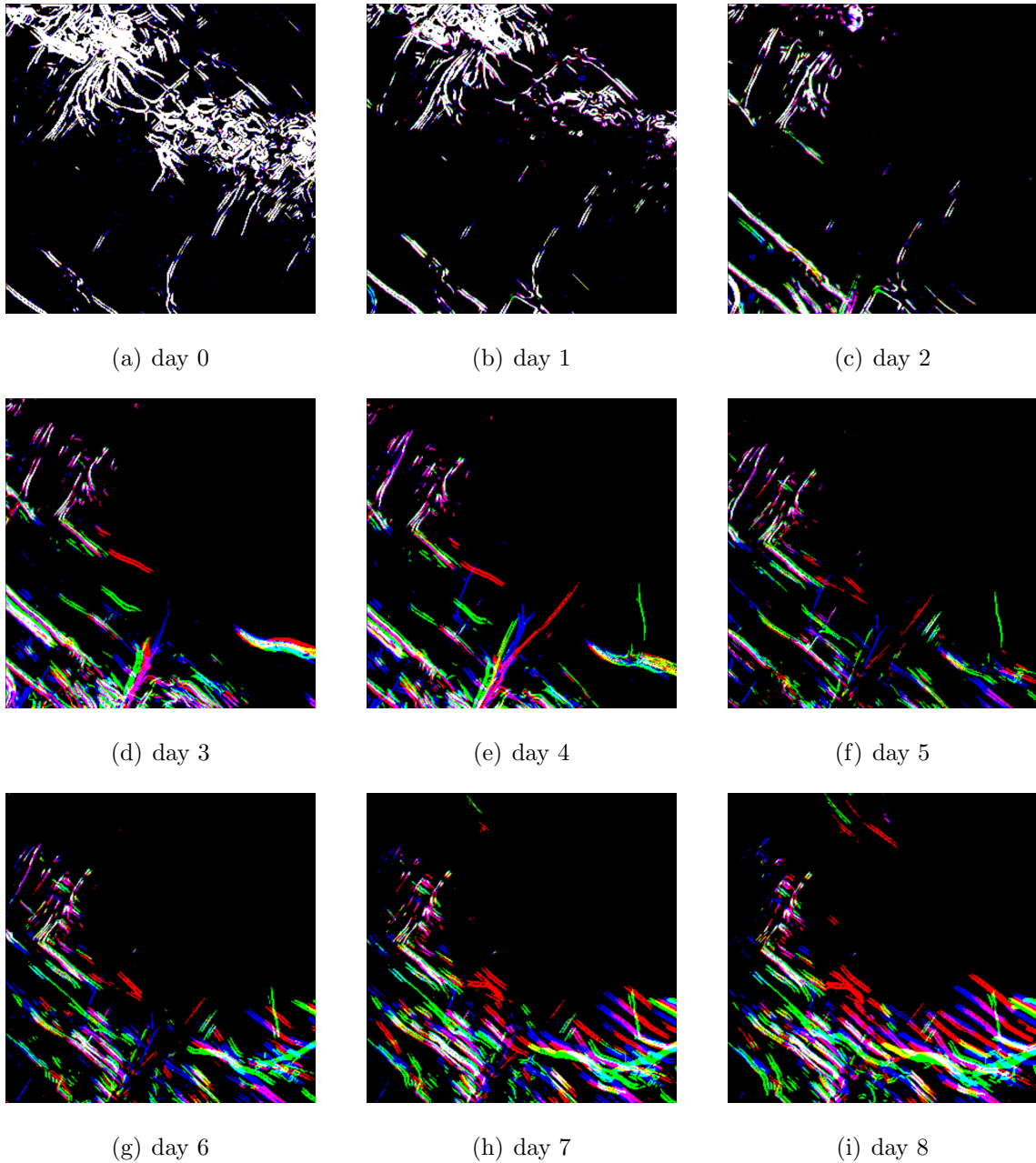
(g) day 6   (h) day 7   (i) day 8

Figure C.1: Time series of masked LKFs in the modeled sea ice of three predictability experiments as RGB image. The sensitivity of the masked LKFs on uncertainties in the initial sea ice concentration (see Section 7.2.1) is shown. The red channel represents the reference run, the green channel an increase of initial sea ice concentration of 1 %, and the blue channel a randomly perturbation of the initial sea ice concentration of 1 %.

Bibliography

Asplin, M. G., Galley, R., Barber, D. G., Prinsenberg, S., 2012. Fracture of summer perennial sea ice by ocean swell as a result of Arctic storms. Journal of Geophysical Research: Oceans 117 (C6), 1–12, c06025.

Bauer, P., Thorpe, A., Brunet, G., 2015. The quiet revolution of numerical weather prediction. Nature 525, 47–55.

Blanchard-Wrigglesworth, E., Bitz, C. M., Holland, M. M., 2011. Influence of initial conditions and climate forcing on predicting Arctic sea ice. Geophysical Research Letters 38 (18), 1–5, l18503.

Bouchat, A., Tremblay, B., 2014. Energy dissipation in viscous-plastic sea-ice models. Journal of Geophysical Research: Oceans 119 (2), 976–994.

Bouillon, S., Rampal, P., 2015a. On producing sea ice deformation data sets from SAR-derived sea ice motion. The Cryosphere 9 (2), 663–673.

Bouillon, S., Rampal, P., 2015b. Presentation of the dynamical core of neXtSIM, a new sea ice model. Ocean Modelling 91, 23 – 37.

Chevallier, M., Salas y Mélia, D., Voldoire, A., Déqué, M., Garric, G., 2013. Seasonal forecasts of the Pan-Arctic sea ice extent using a GCM-based seasonal prediction system. Journal of Climate 26, 6092–6104.

Coon, M. D., Maykut, G. A., Pritchard, R. S., Rothrock, D. A., Thorndike, A. S., 1974. Modeling the pack ice as an elastic-plastic material. AIDJEX Bull. 24, 1–105.

Curry, J. A., Schramm, J. L., Ebert, E. E., 1995. Sea ice-albedo climate feedback mechanism. Journal of Climate 8, 240–247.

Danilov, S., Wang, Q., Timmermann, R., Iakovlev, N., Sidorenko, D., Kimmritz, M., Jung, T., Schröter, J., 2015. Finite-element sea ice model (FESIM), version 2. Geoscientific Model Development 8 (6), 1747–1761.

Feltham, D. L., 2008. Sea ice rheology. Annual Review of Fluid Mechanics 40 (1), 91–112.

Girard, L., Bouillon, S., Weiss, J., Amitrano, D., Fichefet, T., Legat, V., 2011. A new modeling framework for sea-ice mechanics based on elasto-brittle rheology. Annals of Glaciology 52 (57), 123–132.

Girard, L., Weiss, J., Molines, J. M., Barnier, B., Bouillon, S., 2009. Evaluation of high-resolution sea ice models on the basis of statistical and scaling properties of Arctic sea ice drift and deformation. Journal of Geophysical Research: Oceans 114 (C8), 1–15.

Haas, C., Hendricks, S., Eicken, H., Herber, A., 2010. Synoptic airborne thickness surveys reveal state of Arctic sea ice cover. Geophysical Research Letters 37 (9), 1–5, l09501.

Heil, P., Hibler, W. D., 2002. Modeling the high-frequency component of Arctic sea ice drift and deformation. J. Phys. Oceanogr. 32, 3039–3057.

Hibler, W. D., 1977. A viscous sea ice law as a stochastic average of plasticity. Journal of Geophysical Research 82 (27), 3932–3938.

Hibler, W. D., 1979. A dynamic thermodynamic sea ice model. J. Phys. Oceanogr. 9, 815–846.

Hibler, W. D., 2001. Modeling the formation and evolution of oriented fractures in sea ice. Annals of Glaciology 33 (1), 157–164.

Hibler, W. D., Schulson, E. M., 2000. On modeling the anisotropic failure and flow of flawed sea ice. Journal of Geophysical Research: Oceans 105 (C7), 17105–17120.

Hill, V., Cota, G., 2005. Spatial patterns of primary production on the shelf, slope and basin of the Western Arctic in 2002. Deep Sea Research Part II: Topical Studies in Oceanography 52 (24–26), 3344–3354, the Western Arctic Shelf-Basin Interactions (SBI) ProjectThe Western Arctic Shelf-Basin Interactions (SBI) Project.

Holland, M., Bailey, D., Vavrus, S., 2011. Inherent sea ice predictability in the rapidly changing Arctic environment of the Community Climate System Model, version 3. Climate Dynamics 36 (7-8), 1239–1253.

Holloway, G., Proshutinsky, A., 2007. Role of tides in Arctic ocean/ice climate. Journal of Geophysical Research: Oceans 112 (C4), 1–10, c04S06.

Holton, J. R., Hakim, G. J., 2012. An introduction to dynamic meteorology. International geophysics series. Elsevier Academic Press, Amsterdam, Boston, Heidelberg.

Hutchings, J. K., Heil, P., Hibler, W. D., 2005. Modeling linear kinematic features in sea ice. Monthly Weather Review 133, 3481–3497.

Hutchings, J. K., Heil, P., Steer, A., Hibler, W. D., 2012. Subsynoptic scale spatial variability of sea ice deformation in the western Weddell Sea during early summer. Journal of Geophysical Research: Oceans 117 (C1), 1–16, c01002.

Hutchings, J. K., Hibler, W. D., 2008. Small-scale sea ice deformation in the Beaufort Sea seasonal ice zone. Journal of Geophysical Research: Oceans 113 (C8), 1–10.

Hutchings, J. K., Roberts, A., Geiger, C., Richter-Menge, J., 2011. Spatial and temporal characterization of sea-ice deformation. Annals of Glaciology 52 (57), 360–368.

Kaleschke, L., Tian-Kunze, X., Maaß, N., Mäkynen, M., Drusch, M., 2012. Sea ice thickness retrieval from SMOS brightness temperatures during the Arctic freeze-up period. Geophysical Research Letters 39 (5), 1–5, l05501.

Koenigk, T., Mikolajewicz, U., 2009. Seasonal to interannual climate predictability in mid and high northern latitudes in a global coupled model. Climate Dynamics 32 (6), 783–798.

Kreyscher, M., Harder, M., Lemke, P., Flato, G. M., 2000. Results of the sea ice model intercomparison project: Evaluation of sea ice rheology schemes for use in climate simulations. Journal of Geophysical Research: Oceans 105 (C5), 11299–11320.

Kwok, R., 1998. The RADARSAT geophysical processor system. In: Analysis of SAR Data of the Polar Oceans. Springer Berlin Heidelberg, pp. 235–257.
URL http://dx.doi.org/10.1007/978-3-642-60282-5_11

Kwok, R., 2001. Deformation of the arctic ocean sea ice cover between november 1996 and april 1997: A qualitative survey. In: Dempsey, J., Shen, H. (Eds.), IUTAM Symposium on Scaling Laws in Ice Mechanics and Ice Dynamics. Vol. 94 of Solid Mechanics and Its Applications. Springer Netherlands, pp. 315–322.
URL http://dx.doi.org/10.1007/978-94-015-9735-7_26

Kwok, R., 2002. Sea ice concentration estimates from satellite passive microwave radiometry and openings from SAR ice motion. Geophysical Research Letters 29 (9), 25–1–25–4.

Kwok, R., Cunningham, G. F., 2008. ICESat over Arctic sea ice: Estimation of snow depth and ice thickness. Journal of Geophysical Research: Oceans 113 (C8), 1–17, c08010.

Kwok, R., Hunke, E. C., Maslowski, W., Menemenlis, D., Zhang, J., 2008. Variability of sea ice simulations assessed with RGPS kinematics. Journal of Geophysical Research: Oceans 113 (C11), 1–20, c11012.

Leppäranta, M., 2011. The Drift of Sea Ice. Springer Berlin Heidelberg.

Lindsay, R. W., Rothrock, D. A., 1995. Arctic sea ice leads from advanced very high

resolution radiometer images. Journal of Geophysical Research: Oceans 100 (C3), 4533–4544.

Lindsay, R. W., Stern, H. L., 2003. The RADARSAT geophysical processor system: quality of sea ice trajectory and deformation estimates. J. Atmos. Oceanic Technol. 20, 1333–1347.

Lindsay, R. W., Zhang, J., Rothrock, D. A., 2003. Sea-ice deformation rates from satellite measurements and in a model. Atmosphere-Ocean 41 (1), 35–47.

Losch, M., Fuchs, A., Lemieux, J.-F., Vanselow, A., 2014. A parallel Jacobian-free Newton-Krylov solver for a coupled sea ice-ocean model. Journal of Computational Physics 257, Part A, 901–911.

Losch, M., Menemenlis, D., Campin, J.-M., Heimbach, P., Hill, C., 2010. On the formulation of sea-ice models. Part 1: Effects of different solver implementations and parameterizations. Ocean Modelling 33, 129–144.

Lüpkes, C., Gryanik, V. M., Witha, B., Gryschka, M., Raasch, S., Gollnik, T., 2008. Modeling convection over arctic leads with les and a non-eddy-resolving microscale model. Journal of Geophysical Research: Oceans 113 (C9), 1–17, c09028.

Mandelbrot, B., 1983. The Fractal Geometry of Nature. Henry Holt and Company.

Marko, J. R., Thomson, R. E., 1977. Rectilinear leads and internal motions in the ice pack of the Western Arctic Ocean. Journal of Geophysical Research 82 (6), 979–987.

Marsan, D., Stern, H., Lindsay, R., Weiss, J., Oct 2004. Scale dependence and localization of the deformation of Arctic sea ice. Phys. Rev. Lett. 93, 178501.

Martin, S., Thorndike, A. S., 1985. Dispersion of sea ice in the Bering Sea. Journal of Geophysical Research: Oceans 90 (C4), 7223–7226.

Maslowski, W., Lipscomb, W. H., 2003. High resolution simulations of Arctic sea ice, 1979-1993. Polar Research 22 (1), 67–74.

Maykut, G. A., 1982. Large-scale heat exchange and ice production in the Central Arctic. Journal of Geophysical Research: Oceans 87 (C10), 7971–7984.

Maykut, G. A., 1986. The surface heat and mass balance. In: Untersteiner, N. (Ed.), The Geophysics of Sea Ice. NATO ASI Series. Springer US, pp. 395–463.

MITgcm Group, 2015. MITgcm User Manual.
URL `http://mitgcm.org/public/r2_manual/latest/online_documents/manual.pdf`

Onogi, K., Tsutsui, J., Koide, H., Sakamoto, M., Kobayashi, S., Hatsushika, H., Matsumoto, T., Yamazaki, N., Kamahori, H., Takahashi, K., Kadokura, S., Wada, K., Kato, K., Oyama, R., Ose, T., Mannoji, N., Taira, R., 2007. The JRA-25 reanalysis. Journal of the Meteorological Society of Japan. Ser. II 85 (3), 369–432.

Overland, J., Ukita, J., 2000. Dynamics of Arctic sea ice discussed at workshop. Eos, Transactions American Geophysical Union 81 (28), 309–314.

Overland, J. E., Pease, C. H., 1988. Modeling ice dynamics of coastal seas. Journal of Geophysical Research: Oceans 93 (C12), 15619–15637.

Parkinson, C. L., Washington, W. M., 1979. A large-scale numerical model of sea ice. Journal of Geophysical Research: Oceans 84 (C1), 311–337.

Perovich, D. K., Andreas, E. L., Curry, J. A., Eiken, H., Fairall, C. W., Grenfell, T. C., Guest, P., Intrieri, J., Kadko, D., Lindsay, R. W., McPhee, M. G., Morison, J., Moritz, R. E., Paulson, C. A., Pegau, W. S., Persson, P., Pinkel, R., Richter-Menge, J. A., Stanton, T., Stern, H., Sturm, M., Tucker, W., Uttal, T., 1999. Year on ice gives climate insights. Eos, Transactions American Geophysical Union 80 (41), 481–486.

Rampal, P., Weiss, J., Marsan, D., Bourgoin, M., 2009. Arctic sea ice velocity field: General circulation and turbulent-like fluctuations. Journal of Geophysical Research: Oceans 114 (C10), 1–17, c10014.

Rampal, P., Weiss, J., Marsan, D., Lindsay, R., Stern, H., 2008. Scaling properties of sea ice deformation from buoy dispersion analysis. Journal of Geophysical Research: Oceans 113 (C3), 1–12.

Richter-Menge, J. A., Elder, B. C., 1998. Characteristics of pack ice stress in the Aalaskan Beaufort Sea. Journal of Geophysical Research: Oceans 103 (C10), 21817–21829.

Richter-Menge, J. A., McNutt, S. L., Overland, J. E., Kwok, R., 2002. Relating Arctic pack ice stress and deformation under winter conditions. Journal of Geophysical Research: Oceans 107 (C10), SHE 15–1–SHE 15–13.

Rothrock, D. A., Thorndike, A. S., 1984. Measuring the sea ice floe size distribution. Journal of Geophysical Research: Oceans 89 (C4), 6477–6486.

Schulson, E. M., Duval, P., 2009. Creep and Fracture of Ice. Cambridge University Press, cambridge Books Online.
URL http://dx.doi.org/10.1017/CBO9780511581397

Schulson, E. M., Hibler, W. D., 1991. The fracture of ice on scales large and small: Arctic leads and wing cracks. Journal of Glaciology 37 (127), 319–322.

Schulson, E. M., Hibler, W. D., 2004. Fracture of the winter sea ice cover on the Arctic ocean. Comptes Rendus Physique 5 (7), 753 – 767, ice: from dislocations to icy satellites.

Sigmond, M., Fyfe, J. C., Flato, G. M., Kharin, V. V., Merryfield, W. J., 2013. Seasonal forecast skill of Arctic sea ice area in a dynamical forecast system. Geophysical Research Letters 40 (3), 529–534.

Smith, L. C., Stephenson, S. R., 2013. New Trans-Arctic shipping routes navigable by midcentury. Proceedings of the National Academy of Sciences 110 (13), 1191–1195.

Sornette, D., 2006. Critical Phenomena in Natural Sciences. Springer Berlin Heidelberg.

Squire, V. A., Dugan, J. P., Wadhams, P., Rottier, P. J., Liu, A. K., 1995. Of ocean waves and sea ice. Annual Review of Fluid Mechanics 27 (1), 115–168.

Stern, H. L., Lindsay, R. W., 2009. Spatial scaling of arctic sea ice deformation. Journal of Geophysical Research: Oceans 114 (C10), n/a–n/a, c10017.

Stirling, I., 1997. The importance of polynyas, ice edges, and leads to marine mammals and birds. Journal of Marine Systems 10 (1–4), 9–21.

Thorndike, A. S., Colony, R., 1982. Sea ice motion in response to geostrophic winds. Journal of Geophysical Research: Oceans 87 (C8), 5845–5852.

Tietsche, S., Day, J. J., Guemas, V., Hurlin, W. J., Keeley, S. P. E., Matei, D., Msadek, R., Collins, M., Hawkins, E., 2014. Seasonal to interannual arctic sea ice predictability in current global climate models. Geophysical Research Letters 41 (3), 1035–1043.

Wang, K., Wang, C., 2009. Modeling linear kinematic features in pack ice. Journal of Geophysical Research: Oceans 114 (C12), n/a–n/a.

Wang, W., Chen, M., Kumar, A., 2013. Seasonal prediction of arctic sea ice extent from a coupled dynamical forecast system. Monthly Weather Review 141, 1375–1394.

Weiss, J., 2003. Scaling of fracture and faulting of ice on earth. Surveys in Geophysics 24 (2), 185–227.

Zhang, J., Hibler, W. D., 1997. On an efficient numerical method for modeling sea ice dynamics. Journal of Geophysical Research: Oceans 102 (C4), 8691–8702.

Zhang, J., Hibler, W. D., Steele, M., Rothrock, D. A., 1998. Arctic ice-ocean modeling with and without climate restoring. Journal of Physical Oceanography 28, 191–217.